ACS NANO

www.acsnano.org

A Theranostic Nanozyme for Osteoarthritis Treatment and Glycosaminoglycan-Targeted Diagnosis of Cartilage Pathology

Dongze Mo,[#] Yanbing Wen,[#] Chaoqun Cheng,[#] Xiwen Chen, Qi Sun, Hanjie Zhang, Xueying An, Wanling Liu, Xiaomiao Cui, Yihong Zhang, Quan Wang, Chenxin Zhu, Jiawei Li, Hao Dong,[*] and Hui Wei[*]

Cite This: https://doi.org/10.1021/acsnano.6c15540

Read Online

ACCESS | Metrics & More | Article Recommendations | Supporting Information

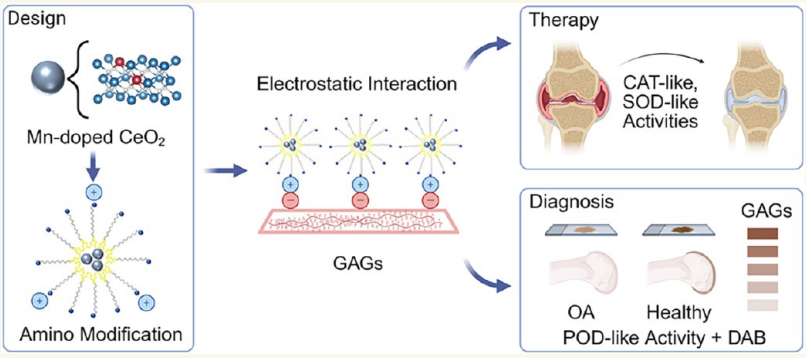

ABSTRACT: **The lack of vascular and neural innervations in cartilage often results in poor drug delivery and penetration, compromising the efficacy of current therapeutics. To tackle this clinical challenge, we designed positively charged manganese-doped CeO_2 nanozymes that combine reactive oxygen species (ROS)-scavenging activity with prolonged retention in the joint cavity by taking advantage of the negatively charged cartilage matrix. Integrating coarse-grained molecular dynamics simulations with experimental validation, we identified chondroitin sulfate as the key glycosaminoglycan responsible for mediating the retention of these positively charged nanozymes in the joint cavity. After intra-articular administration, manganese-doped CeO_2 promoted cartilage defect repair and subchondral bone remodeling in a rat model within 4 weeks. In addition, benefiting from the multiple enzyme mimicking activity of nanozymes, the peroxidase-like activity of manganese-doped CeO_2 was explored to develop a pathological assay to detect the state of cartilage repair. This study establishes an integrated framework combining theoretical modeling with experimental validation to elucidate intra-articular retention mechanisms. The framework enables the rational design of theranostic nanozymes that exploit disease-specific pathological features for both diagnosis and therapy.**

KEYWORDS: *nanozymes, osteoarthritis, cartilage, pathology diagnosis, molecular dynamics*

INTRODUCTION

Amid global population aging, approximately 607 million people are affected by osteoarthritis (OA), and the global disease burden continues to increase.[1] OA is a common joint disease that causes progressive degeneration of articular cartilage.[2] Cartilage damage results in severe pain and markedly impairs patients' daily activities.[3] Cartilage injury is accompanied by inflammation and elevated levels of reactive oxygen species (ROS). Excessive levels of ROS impair the growth and function of chondrocytes.[4] Existing therapeutic agents used clinically for cartilage injuries mainly include corticosteroids and nonsteroidal anti-inflammatory drugs.[5] Due to the lack of vascular structures surrounding articular cartilage, these drugs cannot accurately reach the peri-cartilage region

Received: August 12, 2026
Revised: September 5, 2026
Accepted: September 8, 2026

Scheme 1. Schematic Illustration of Positively Charged Mn-Doped CeO_2 Nanozyme for Osteoarthritis Treatment and Cartilage Pathology Detection[a]

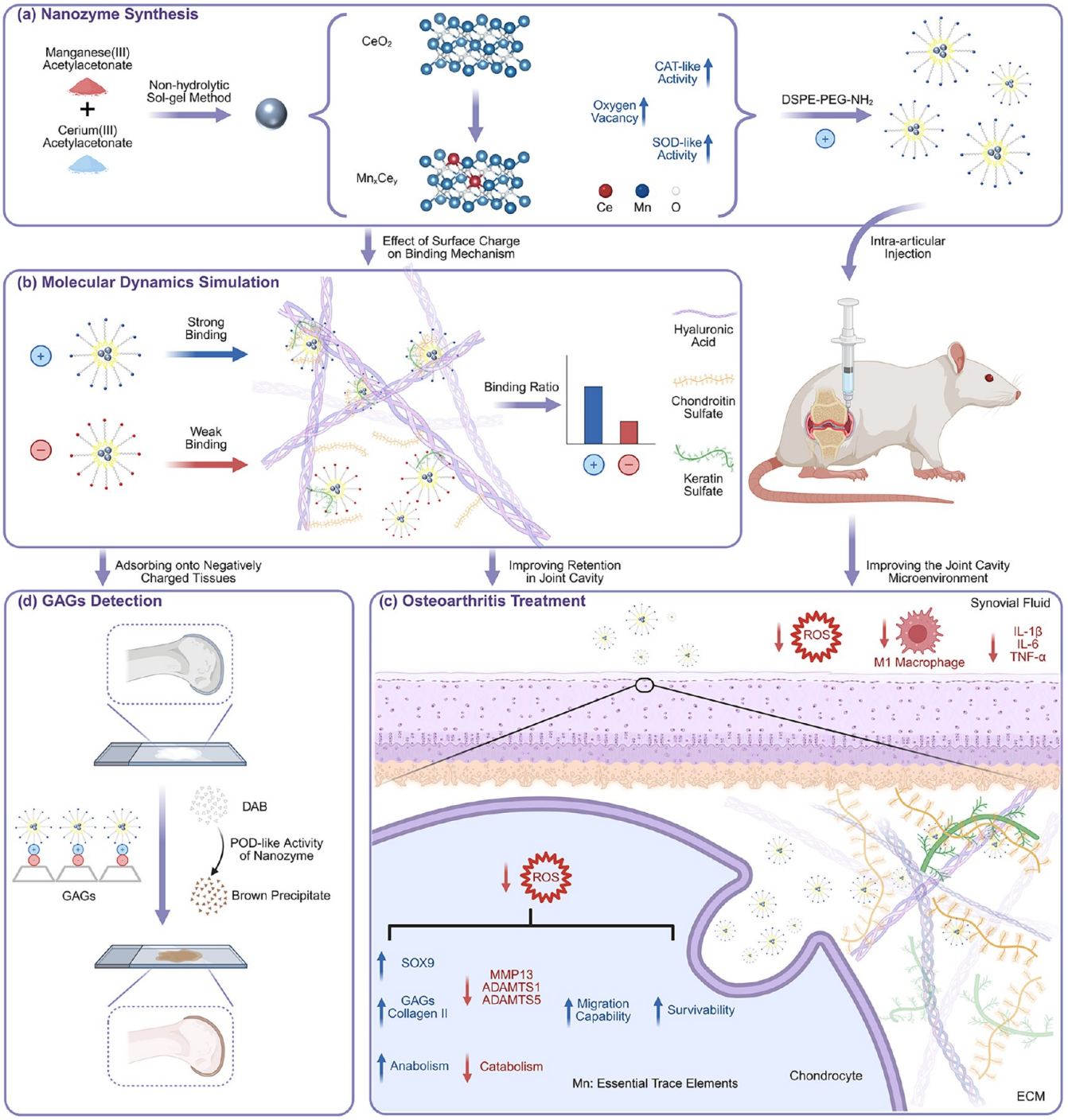

[a](a) Mn-doped CeO_2 modulates enzyme-like catalytic activity based on oxygen vacancy content. (b) Molecular dynamics simulation reveals the effect of charge on the binding strength between nanozymes and GAGs. (c) Nanozyme treats inflammation in macrophages and chondrocytes within joint cavity, relieving osteoarthritis. (d) Positively charged nanozyme visualizes GAGs in cartilage sections using POD-like activity for pathology diagnosis.

through intravenous injection.[6] Intra-articular injections are often chosen clinically to improve the bioavailability of the drug in the joint cavity environment.[7] However, it remains difficult to sustain therapeutic concentrations around chondrocytes.[8] They are rapidly lost through synovial capillaries and lymphatic drainage with intra-articular residence times of only 1−4 h.[9] Meanwhile, cartilage is surrounded by abundant glycosaminoglycans (GAGs), collagen fibers, and other proteins.[10] The cartilage extracellular matrix (ECM) is densely negatively charged and contains pores of 60−200 nm. Consequently, the limited amount of drug retained in the joint is further hindered by the cartilage extracellular matrix, restricting its penetration to chondrocytes and compromising therapeutic efficacy.[11] Furthermore, frequent drug injections to

https://doi.org/10.1021/acsnano.6c15540
ACS Nano XXXX, XXX, XXX−XXX

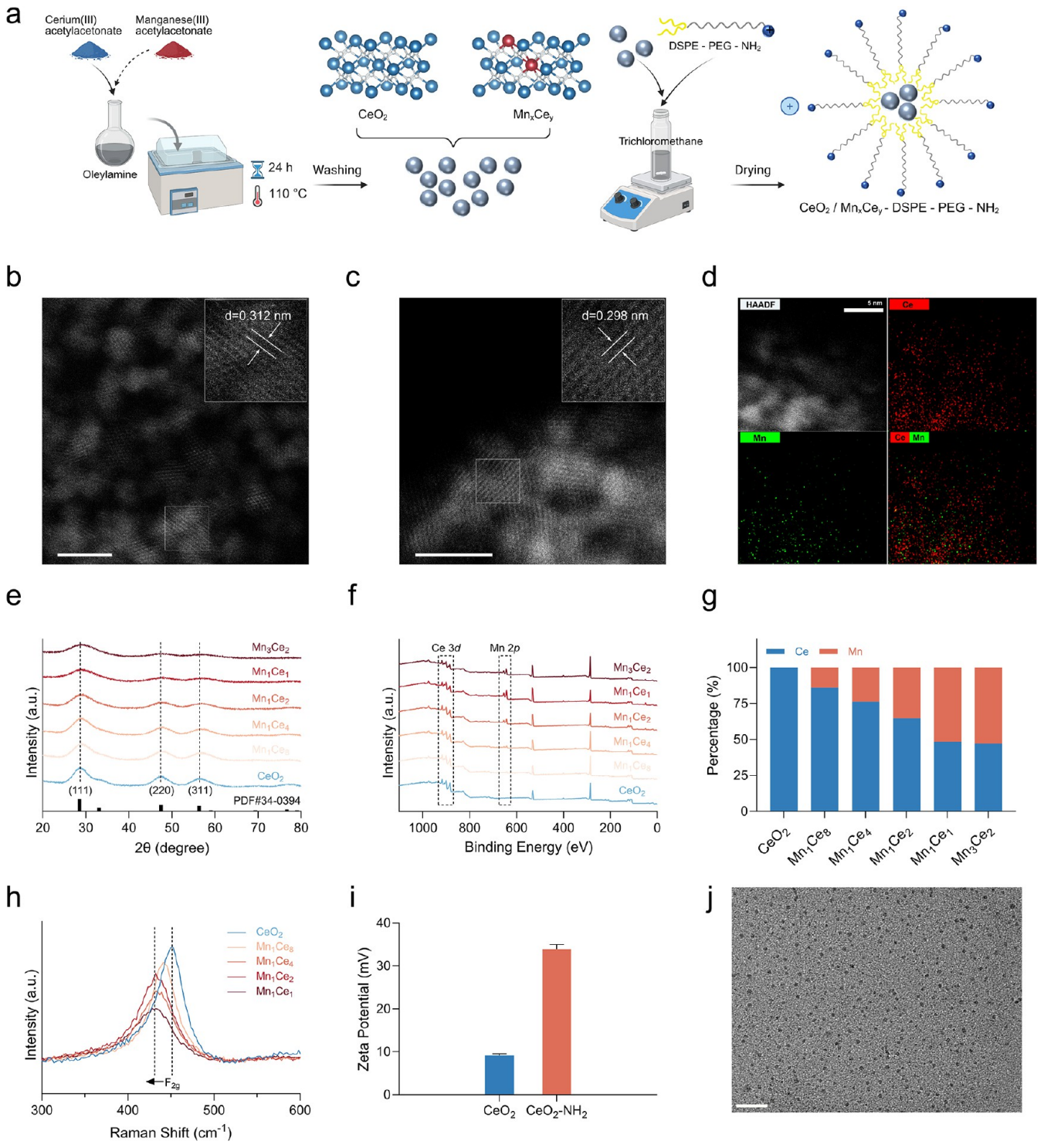

Figure 1. Synthesis and characterization of Mn_xCe_y nanozymes. (a) Schematic of positively charged Mn_xCe_y nanozyme synthesis. AC-HAADF-STEM images of (b) CeO_2 and (c) Mn_1Ce_2 (scale bar: 5 nm). (d) EDS mapping images of Mn_1Ce_2. (e) XRD patterns of Mn_xCe_y. (f) XPS survey scan of Mn_xCe_y. (g) Contents of Mn and Ce in Mn_xCe_y nanozymes measured by ICP−OES. (h) Raman spectra of Mn_xCe_y. (i) Zeta potentials of nanozyme with or without amino group modification. (j) TEM image of phospholipid-modified nanozyme (scale bar: 20 nm).

maintain effective drug concentrations may result in an unacceptably high risk of clinical infections and a reduced quality of life for patients.[12]

Facing these barriers, cationic agents offer distinct advantages: in the negatively charged environment of the joint cavity, they exhibit a longer retention time and achieve effective penetration. Recently, Chen et al. found that cationic particles specifically bind to chondroitin sulfate (CS) and heparan sulfate (HS) in the extracellular matrix through electrostatic interactions, thereby promoting the aggregation and retention of GAGs.[13] Furthermore, low-dose intra-articular injection of cationic polymers does not induce inflammatory

https://doi.org/10.1021/acsnano.6c15540
ACS Nano XXXX, XXX, XXX−XXX

responses or systemic toxicity; rather, it improves the homeostasis of the cartilage matrix. In a related strategy, researchers designed positively charged nanocarriers to encapsulate small-molecule drugs, which can similarly prolong the retention time of these molecules, overcome delivery barriers, and facilitate their effective penetration.[14] In a recent report, insulin-like growth factor 1 (IGF-1) was encapsulated in positively charged PEGylated dendrimers, which prolonged its intra-articular retention 10-fold compared to free IGF-1.[15] Similarly, an antioxidant drug, gallic acid, was loaded into positively charged nanoliposomes, which were subsequently assembled into adhesive hydrogel microspheres. Following intra-articular injection, the microspheres effectively penetrated the cartilage matrix and released gallic acid for therapy.[16] In addition, rapamycin-liposome-incorporating hyaluronic acid–based hydrogel microspheres improved joint lubrication and released rapamycin (an autophagy activator)-loaded cationic liposomes. The cationic liposomes selectively targeted negatively charged cartilage, which reduced off-target accumulation in other joint tissues.[17] Although small-molecule drugs can scavenge ROS or promote cartilage regeneration, their efficacy is often constrained by rapid consumption during therapeutic action, while biological proteins and natural antioxidant enzymes face additional limitations, including poor structural stability, susceptibility to degradation, short biological half-lives, and potential immunogenicity. Therefore, innovative therapeutic strategies to scavenge ROS, inhibit inflammation, and promote cartilage regeneration are still urgently needed.

Recently, nanozymes, nanomaterials with enzyme-like activities, have been developed and applied in bioanalysis, diagnosis, and therapeutics due to their advantages over natural enzymes and conventional enzyme mimics, such as low cost, high stability, multiple enzyme-like activities under different conditions, and compositional diversity and tunable catalytic activities.[18−23] In particular, anti-oxidant nanozymes have been explored for anti-inflammatory therapy, including the treatment of OA.[24] Among these, ceria nanozymes (CeO_2) have garnered significant attention owing to their excellent biocompatibility and their superoxide dismutase (SOD)- and catalase (CAT)-like activities, which enable them to effectively eliminate two representative pathological ROS, $^{\bullet}O_2^-$ and H_2O_2.[25−27] Importantly, their enzyme-like activities can be tuned by doping.[28,29] For example, the Zr^{4+}-doped CeO_2 enhanced the catalytic performance in scavenging ROS by controlling the Ce^{3+} to Ce^{4+} ratio.[30] Additionally, it is noteworthy that manganese supplementation plays a crucial role in the development of bones and cartilage.[31−34] Mn^{2+} contributes to cartilage matrix homeostasis by acting as a cofactor for glycosyltransferases required for GAG biosynthesis, while also modulating cell–matrix adhesion through the regulation of integrin conformation and ligand-binding affinity.[35−37] Therefore, we hypothesize that CeO_2 nanozymes, through the doping of Mn ions, may achieve enhanced catalytic activity, exhibit excellent biocompatibility in bone and cartilage environments, and provide significant benefits for cartilage regeneration.

In this work, we rationally designed and synthesized Mn-doped CeO_2 nanozymes (Mn_xCe_y) *via* a controlled doping strategy (Scheme 1). The doping of low-valence Mn ions into the CeO_2 lattice induced a synergistic effect of oxygen vacancies and electronic modulation, which not only optimized charge transfer kinetics but also created abundant surface-active sites. This structural synergy endowed Mn_xCe_y with dual enzyme-mimetic activities (SOD and CAT), enabling robust scavenging of pathological ROS. We further screened Mn_1Ce_2, which exhibited both excellent antioxidant activity and biocompatibility, and verified the therapeutic effect of Mn_1Ce_2 in alleviating cartilage degeneration and OA. To elucidate the molecular mechanisms governing nanozyme-cartilage interactions, we performed coarse-grained molecular dynamics (CGMD) simulations incorporating both cationic and anionic nanozymes (~6 nm diameter) within a physiologically relevant cartilage extracellular matrix model containing GAGs. Comprehensive trajectory analysis revealed distinct retention tendencies, binding preferences, and binding modes, and identified CS as the critical GAG species responsible for sustained nanozyme retention within the joint cavity. Importantly, by leveraging the unique physicochemical properties of Mn_1Ce_2, including its cationic surface charge for cartilage-targeted retention and peroxidase (POD)-like activity for GAGs visualization, we established a facile yet sensitive diagnostic platform for cartilage pathology detection. This study highlighted the dual potential of Mn-doped CeO_2 nanozymes as both a therapeutic agent for OA and a diagnostic tool for cartilage defect detection.

RESULTS AND DISCUSSION

Synthesis and Characterization of Mn-Doped CeO_2 Nanozyme

Mn-doped CeO_2 nanozymes were synthesized *via* a non-hydrolytic sol-gel method by using oleylamine (OAm) as a capping agent (Figure 1a). They were named Mn_xCe_y, where x and y represent the ratio of the molar amounts of the two precursors. To demonstrate whether Mn ions were successfully doped into the CeO_2 lattice, aberration-corrected high-angle annular dark-field scanning transmission electron microscopy (AC-HAADF-STEM) was used to obtain the lattice spacing information. The (111) lattice spacing of Mn_1Ce_2 was measured to be 0.298 nm, smaller than that of CeO_2 (0.312 nm) (Figure 1b,c). This lattice contraction was attributed to the substitution of Ce ions by Mn ions with smaller ionic radii.[38] Energy dispersive spectra (EDS) showed a uniform distribution of Ce and Mn elements in Mn_1Ce_2, indicating that Mn did not form localized aggregates (Figure 1d). Figure S1 showed the distribution of Ce elements in CeO_2. As shown in Figure 1e, the powder X-ray diffraction (PXRD) patterns of Mn_xCe_y nanozymes were recorded to study their crystalline properties. The presence of broad diffraction peaks ((111), (220), and (311) reflections) confirmed the formation of ceria with a cubic fluorite structure. The absence of additional reflections indicated that no crystalline Mn or Mn oxide phases were formed. The peaks of the samples gradually showed a slight shift towards higher Bragg angles after doping of Mn in the ceria lattice. Such shift is also indicative of the replacement of Ce ions in the cubic fluorite structure by Mn ions with smaller ionic radius.[38] In addition, the doping of Mn also leads to a decrease in the crystallinity of the ceria lattice, resulting in a gradual decrease in diffraction peak intensity. Besides, electron paramagnetic resonance (EPR) illustrated the doping of Mn elements from the perspective of magnetic enhancement (Figure S2).[39] The relative peaks of Ce 3*d* and Mn 2*p* in X-ray photoelectron spectroscopy (XPS) qualitatively confirmed the content of Ce and Mn elements in the doped samples (Figure 1f). As shown in Figure 1g, we quantified the Ce and Mn

https://doi.org/10.1021/acsnano.6c15540
ACS Nano XXXX, XXX, XXX−XXX

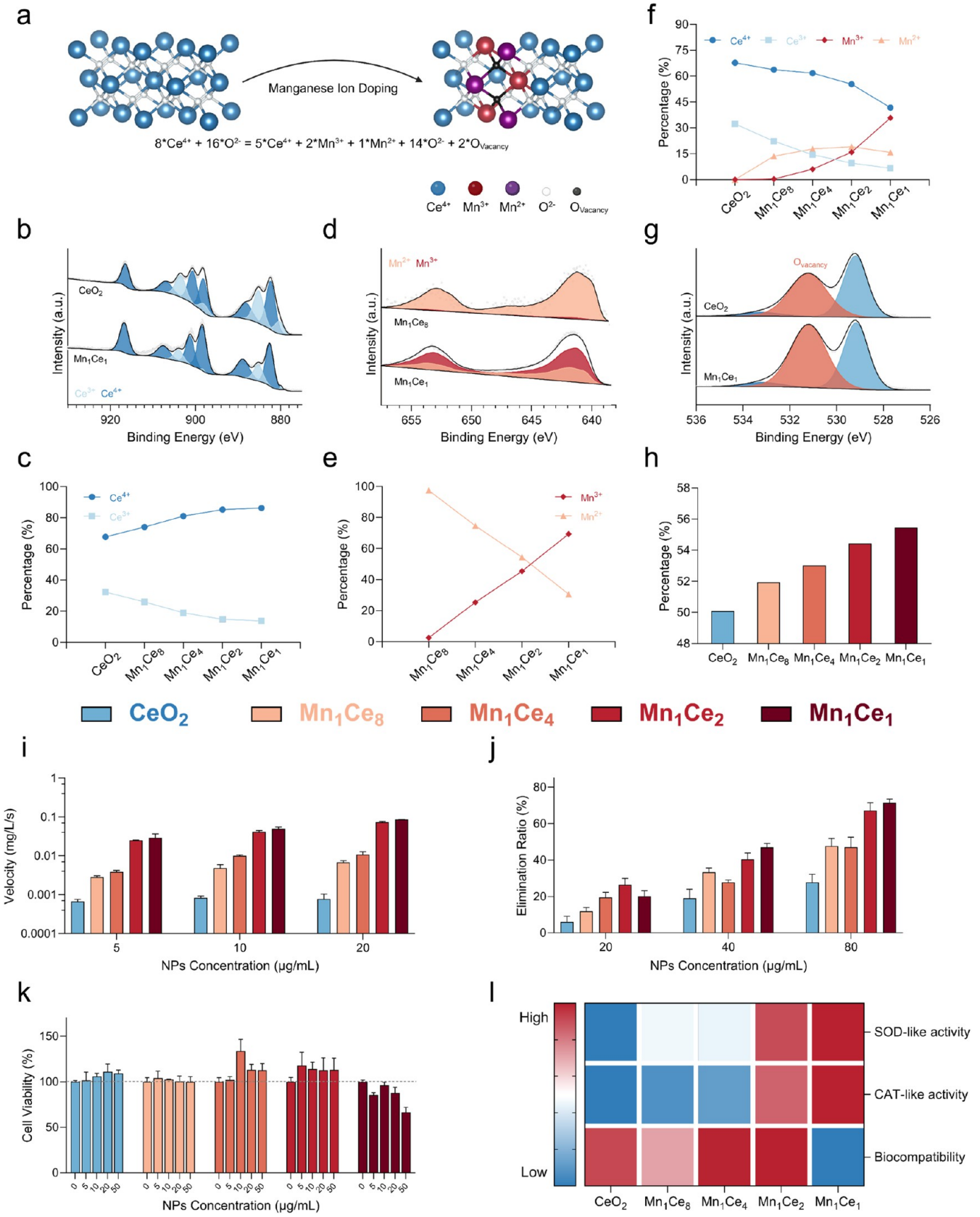

Figure 2. Measurement of oxygen vacancies and enzyme-like activities of Mn_xCe_y nanozymes. (a) Schematic illustration of Mn ion doping into the ceria lattice. In the fluorite structure, ions at corners/edges/faces are shared by adjacent unit cells (corner: 1/8, edge: 1/4, face: 1/2, body: 1). (b) Ce 3d of CeO_2 and Mn_1Ce_1. (c) Percentage of Ce^{3+} and Ce^{4+} to overall Ce ions of Mn_xCe_y. (d) Mn 2*p* of Mn_1Ce_8 and Mn_1Ce_1. (e) Percentage of Mn^{2+} and Mn^{3+} to overall Mn ions of Mn_xCe_y. (f) Percentage of Ce^{3+}, Ce^{4+}, Mn^{2+} and Mn^{3+} to overall metal cations of Mn_xCe_y. (g) O 1*s* of CeO_2 and Mn_1Ce_1. (h) Percentage of oxygen vacancies of Mn_xCe_y. (i) Rate of dissolved oxygen generation from H_2O_2

https://doi.org/10.1021/acsnano.6c15540
ACS Nano XXXX, XXX, XXX−XXX

Figure 2. continued

catalyzed by Mn_xCe_y nanozymes. (j) Measurement of $^{\bullet}O_2^-$ elimination of Mn_xCe_y nanozymes. (k) Cell viability of RAW 264.7 cells after incubation with different concentrations of nanozymes. (l) Schematic of performance evaluation of Mn_xCe_y nanozymes. Data are presented as mean ± standard error of the mean (n = 3).

contents in the doped samples using inductively coupled plasma optical emission spectrometer (ICP-OES). XPS and ICP showed that the Mn content increased, whereas the Ce content decreased with increasing x:y ratios. The measured percentages of Mn and Ce in several products were in good agreement with the initial Mn/Ce molar ratios, such as Mn_1Ce_8, Mn_1Ce_4, Mn_1Ce_2 and Mn_1Ce_1. However, for Mn_3Ce_2, not all of the initially added Mn was successfully incorporated into the product, indicating that the Mn doping limit had been reached under these synthesis conditions. Therefore, Mn_3Ce_2 was not further included in the subsequent characterization due to the similar Mn percentage as Mn_1Ce_1 and its low crystallinity. As shown in the Raman spectra, a dominant peak F_{2g} centered at 450 cm^{-1} was observed in CeO_2, which originated from the symmetric stretching vibration of the O atoms around the Ce atoms.[40,41] However, the F_{2g} peaks in Mn_xCe_y were all red-shifted and broadened, which was attributed to the doping-induced change in lattice size and increase in crystal structure disorder (Figure 1h).[42,43] In addition, there were no vibration peaks related to manganese oxide in the Raman spectra of the Mn_xCe_y.

The nanozymes were then coated with DSPE-PEG-NH_2, a phospholipid derivative selected because its amphiphilic phospholipid structure enables effective surface coating, while the PEG segment improves aqueous dispersibility and colloidal stability. In addition, the terminal amino groups confer a positively charged surface, which facilitates electrostatic interactions with negatively charged GAGs in the cartilage extracellular matrix. Dynamic light scattering (DLS) showed that the nanozymes exhibited a more positive surface potential after coating with phospholipids, which was attributed to the introduction of amino groups (Figure 1i). The zeta potentials of the other Mn_xCe_y were all around +30 mV (Figure S3). TEM image showed that the particle sizes of Mn_1Ce_2 after phospholipid modification are similar, at approximately 5 nm (Figure 1j). Photographs of the aqueous nanozyme dispersions are shown in Figure S4. With increasing Mn doping, the color of the nanozyme dispersion gradually darkened. In summary, we synthesized a Mn-doped CeO_2 nanozyme with good water dispersibility and uniform particle size.

Measurement of Oxygen Vacancies and Enzyme-like Activities of Mn-Doped CeO_2 Nanozyme

We constructed a possible structural model in which Mn ions were incorporated into the ceria lattice (Figure 2a). As lower-valence Mn ions substitute for Ce ions, the average metal valence decreases, leading to the formation of additional oxygen vacancies to maintain charge neutrality. As the amount of Mn doping increases, the percentage of Ce^{3+} decreases while Ce^{4+} increases (Figures 2b,c and S5). The increase of the valence state of Ce ions may arise from partial electron transfer from Ce^{3+} to Mn^{3+}, generating more Ce^{4+} and Mn^{2+}. For Mn ions, the percentage of Mn^{2+} decreases and Mn^{3+} increases (Figures 2d,e and S6). The manganese acetylacetonate precursor used here contains Mn^{3+}, so the Mn^{2+} in the product is created by gaining electrons from the Ce ion. With increasing amounts of the Mn^{3+} precursor, the electron-donating capacity of Ce^{3+} becomes insufficient to fully reduce the precursor, resulting in a gradual increase in the proportion of Mn^{3+} in the product. We calculated the overall metal ion distribution based on the elemental occupancy results obtained by ICP and the ion valence occupancy results obtained by XPS (Figure 2f). The percentage of tetravalent cations decreases, while the percentage of trivalent and divalent cations increases. The calculated average valence of the total metal cations (Ce and Mn) decreased from +3.68 to +3.26 (Figure S7). As shown in Figures 2g,2h, and S8, the oxygen vacancy ratio derived from the O 1s spectra gradually increased, which was consistent with the structural model proposed in Figure 2a.

To verify whether oxygen vacancies can optimize the electronic structure and enhance the catalytic performance of the nanozymes, we selected two representative ROS, H_2O_2 and $^{\bullet}O_2^-$, to investigate the CAT- and SOD-like activities. CAT-like activity was measured using the rate of O_2 production from H_2O_2 catalyzed by nanozymes (Figure 2i). The corresponding dissolved oxygen profiles are shown in Figure S9. In addition, we used the dopamine method to determine the absolute CAT-like activity of the nanozyme (Figure S10). SOD-like activity of Mn_xCe_y nanozymes was studied by monitoring the $^{\bullet}O_2^-$ elimination with a SOD assay kit (Figure 2j). Our measurements at multiple concentrations demonstrated a consistent trend in oxygen vacancy occupancy and enzyme-like activity. Mn_1Ce_1, which exhibited the highest oxygen-vacancy percentage, showed about 3-fold enhancement of SOD-like activity and nearly 100-fold enhancement of CAT-like activity compared with CeO_2. Furthermore, the biocompatibility of Mn_xCe_y nanozymes was evaluated, which is also crucial for biomedical applications. We performed a cell viability assay with RAW 264.7 cells to investigate the cytocompatibility of Mn_xCe_y nanozymes. As shown in Figure 2k, cell viability remained above 100% after 24 h of incubation with 0−50 μg/mL CeO_2, Mn_1Ce_8, Mn_1Ce_4, and Mn_1Ce_2. However, for Mn_1Ce_1, cell viability decreased across the tested concentration range, which could be attributed to an abnormal cellular immune response induced by excess Mn ions.[44] Meanwhile, we performed live−dead staining on RAW 264.7 cells under identical conditions, demonstrating that CeO_2 and Mn_1Ce_2 exhibited no significant cytotoxicity, whereas Mn_1Ce_1 caused visible cell death (Figure S11). Considering the above three indicators, we selected Mn_1Ce_2 for subsequent therapeutic studies due to its strong ROS scavenging activity and excellent biocompatibility (Figure 2l). To comprehensively assess the ROS scavenging capacity of Mn_1Ce_2, we further investigated its hydroxyl radical ($^{\bullet}OH$) elimination capability. The results revealed that Mn_1Ce_2 scavenged 23.29% of $^{\bullet}OH$ within 3 min, whereas CeO_2 showed only 6.18% scavenging activity (Figure S12). In addition, nitrogen radical scavenging assays with DPPH$^{\bullet}$ and ABTS$^{+\bullet}$ are frequently used to evaluate the reactive nitrogen species (RNS) scavenging activity of nanozymes. We found that the Mn_1Ce_2 also possessed superior RNS scavenging activity than CeO_2, which also contributes to the elimination of inflammatory reactions in organisms (Figure S13).

https://doi.org/10.1021/acsnano.6c15540
ACS Nano XXXX, XXX, XXX−XXX

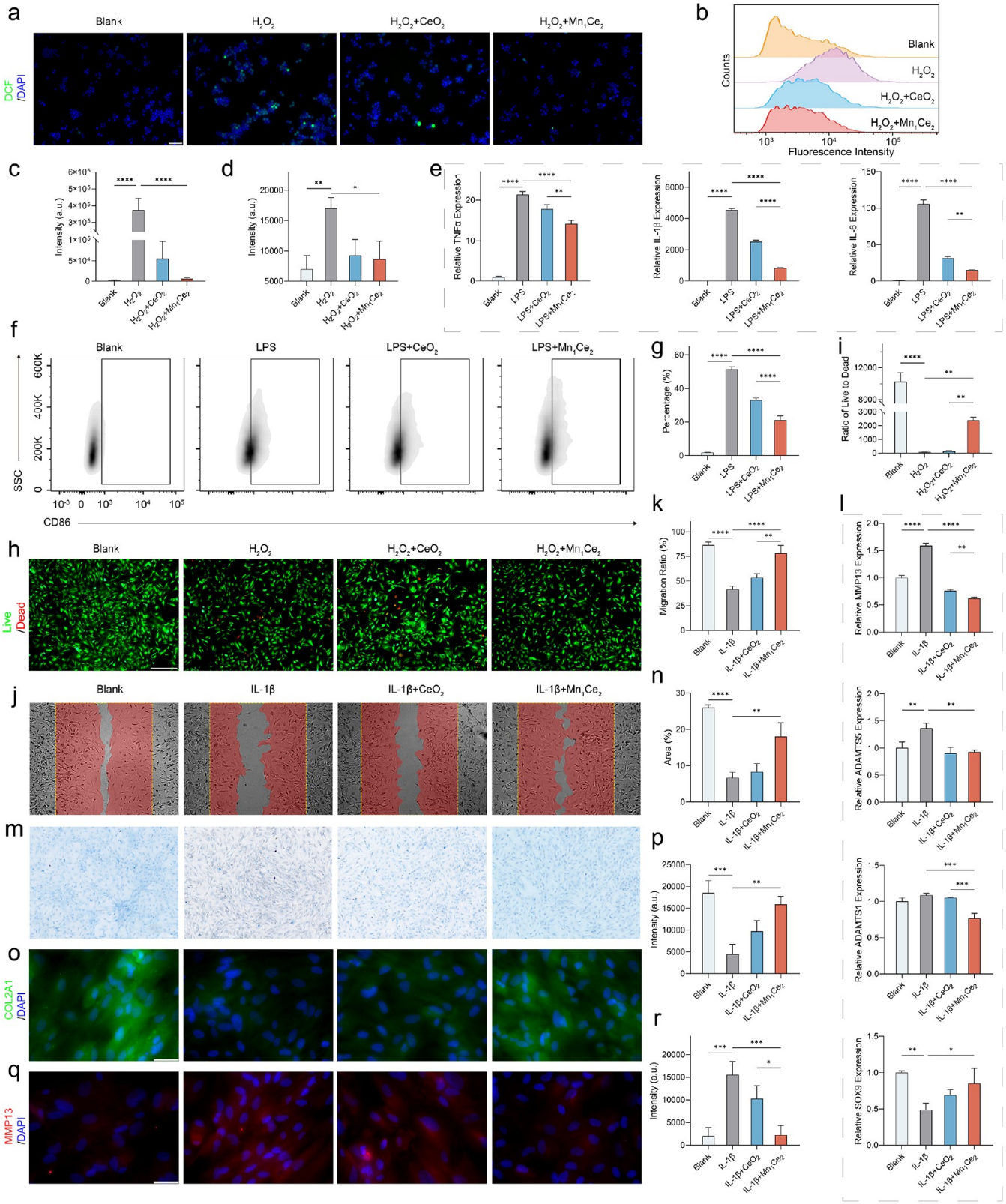

Figure 3. *In vitro* OA treatment effect of Mn-doped CeO_2 nanozyme. ROS level of RAW 264.7 cells monitored by (a) laser scanning confocal microscopy (scale bar: 100 μm) and (b) flow cytometer in the presence or absence of nanozymes. Quantification of ROS levels detected by (c) laser scanning confocal microscopy and (d) flow cytometer in differently treated macrophages. (e) Relative gene expression of pro-inflammatory cytokines (TNFα, IL-1β, and IL-6) from macrophages. (f) Flow cytometric analysis of the expression levels of M1 macrophages ($CD86^+$/ SSC) and (g) quantitative analysis of the average optical density of $CD86^+$/ SSC. (h) Staining of live and dead cells in different culture conditions (scale bar: 500 μm). (i) Quantification of live−dead cell staining. (j) Bright-field image of cell migration after 24 h of scratching (scale bar: 800 μm). (k) Migration ratio quantified from scratch test. (l) Relative mRNA expression levels of cartilage matrix metabolism (MMP13, ADAMTS5, ADAMTS1, and SOX9) in chondrocytes. (m) Staining of cartilage matrix by Alcian Blue (scale bar: 200

https://doi.org/10.1021/acsnano.6c15540
ACS Nano XXXX, XXX, XXX−XXX

Figure 3. continued

μm) and (n) its quantitative analysis. (o) Immunofluorescence staining of COL2A1 (scale bar: 50 μm) and (p) its quantitative analysis. (q) Immunofluorescence staining of MMP13 (scale bar: 50 μm) and (r) its quantitative analysis. Data are presented as mean ± standard error of the mean (n = 3). Statistical analysis was performed using one-way ANOVA, *p < 0.05, **p < 0.01, ***p < 0.001, ****p < 0.0001.

In Vitro OA Treatment Effect of Mn-Doped CeO_2 Nanozyme

To evaluate the storage stability of Mn_1Ce_2, we monitored its hydrodynamic diameter and zeta potential during storage in deionized water at 25 °C. The hydrodynamic diameters were 52.7, 84.5, and 156.4 nm on days 0, 14, and 60, respectively, while the corresponding zeta potentials were +33.8, +30.4, and +26.3 mV (Figure S14). Although the gradual increase in hydrodynamic diameter suggested some degree of particle association during prolonged storage, Mn_1Ce_2 retained a positively charged surface throughout the 60-day observation period, with a relatively small change in zeta potential during the first 14 days. To further assess the stability of Mn_1Ce_2 and the potential toxicity associated with excessive Mn ion release, we monitored Mn ion release over 48 h (Figure S15). The results showed that 5 mg of Mn_1Ce_2 (containing 500 μg of Mn) released 14.43 μg of Mn at 24 h and 15.34 μg at 48 h, corresponding to approximately 3% of the total Mn content. The initial release within 24 h may be attributed to the dissolution of a small amount of surface-associated Mn ions. Low concentrations of Mn ions in the joint synovial fluid may be beneficial for bone and cartilage regeneration.[31,36] Notably, only a small additional amount of Mn was released between 24 and 48 h, suggesting that the release profile had approached a plateau and that most of the Mn remained stably incorporated within the Mn_1Ce_2 nanozyme. Taken together, these results indicate that Mn_1Ce_2 maintains its positively charged surface during storage and exhibits limited Mn ion release, supporting its physicochemical stability for subsequent biological applications.

The osteoarthritic environment is accompanied by macrophage M1 phenotypic polarization and excess ROS production, which affects normal chondrocyte function.[45,46] A vicious cycle develops between increased inflammation and cartilage matrix breakdown, leading to progressive OA severity.[47] To assess whether Mn_1Ce_2 could interrupt this vicious cycle, we validated its ability to scavenge ROS and induce macrophage polarization. Macrophage ROS levels were measured by the ROS fluorescent probe 2',7'-dichlorodihydrofluorescein diacetate (DCFH-DA). As shown in Figure 3a,3c, H_2O_2 treatment of RAW 264.7 cells resulted in a significant enhancement of the green fluorescence level of the cells, indicating that the intracellular ROS level was elevated. Treatment with CeO_2 and Mn_1Ce_2 down-regulated the ROS level. We further validated this result using flow cytometry (Figure 3b,d). To validate the ability of the nanozyme to inhibit macrophage M1 polarization, the mRNA expression levels of pro-inflammatory cytokines in different groups were quantitatively assessed by reverse transcription-polymerase chain reaction (RT-PCR) (Figure 3e). After lipopolysaccharide (LPS) stimulation, mRNA expression of TNFα, Interleukin-6 (IL-6), and IL-1β was significantly up-regulated 21-fold, 105-fold, and 4532-fold, respectively. Both CeO_2 and Mn_1Ce_2 nanozymes resulted in a significant decrease in M1 markers. Notably, Mn_1Ce_2 produced a more pronounced downregulation, indicating a superior anti-inflammatory effect, which is consistent with the results of our evaluation for enzyme-like activities. Furthermore, LPS-stimulated RAW 264.7 cells were co-incubated with the nanozyme, and M1 macrophages were identified by staining with an anti-CD86 antibody (Figure 3f,g). Flow cytometry analysis showed that LPS markedly promoted macrophage polarization toward the M1 phenotype, whereas Mn_1Ce_2 significantly suppressed M1 polarization.

We further explored whether Mn-doped CeO_2 nanozyme can restore chondrocyte function under oxidative stress. The cytotoxicity of nanozymes on rat chondrocytes was evaluated by cell counting kit-8 (CCK-8) assay. After co-incubation with CeO_2 and Mn_1Ce_2 for 24 h, there was no decrease in cell viability of chondrocytes, which indicated the potential for biological application in the joint environment (Figure S16). We then investigated the cytoprotective effects of these two nanozymes through live−dead staining of chondrocytes (Figure 3h). No red fluorescence reflecting cell death was observed in the blank group. In the group with H_2O_2, there was a decrease in green fluorescence of living cells and an increase in red fluorescence. Compared with CeO_2, Mn_1Ce_2 nanozymes significantly alleviated the oxidative stress-induced cell death. As shown in Figure 3i, the ratio of fluorescence intensity of living cells to that of dead cells in different groups quantitatively confirmed the superior cytoprotective effect of Mn_1Ce_2. In addition, we found that the nanozyme could restore the migration function of chondrocytes under OA. The restoration of the migration function of chondrocytes contributes to the repair of cartilage defects.[48,49] We created *in vitro* wounds by scratching the cell monolayer with a standardized pipette tip under different incubation conditions. IL-1β is widely used to construct experimental OA models of chondrocytes.[50] Figures 3j and S17 showed the bright field images of the cell distribution of different groups at 0 h (at the time of wounding) and after 24 h. Among them, the IL-1β-induced group showed the weakest migratory ability, while the Mn_1Ce_2 and control groups almost reached confluence. The results of the migration rate calculated using the area of the cell-free region were consistent with these observations (Figure 3k).

Anabolism and catabolism of the cartilage matrix maintain the balance of the physiological environment in the joint.[51] The progression of OA is closely related to the overactive catabolism of the cartilage matrix. A disintegrin and metalloproteinase with thrombospondin motifs (ADAMTS)1, ADAMTS5, and matrix metalloproteinase (MMP)13 are involved in proteoglycan degradation, which further leads to progressive destruction of the cartilage matrix.[52] The results of RT-PCR showed that IL-1β stimulation activated catabolic processes in cartilage and induced the up-regulation of ADAMTS5, ADAMTS1 and MMP13 in chondrocytes (Figure 3l). Both CeO_2 and Mn_1Ce_2 reversed these changes, with Mn_1Ce_2 being more effective. SRY-related protein 9 (SOX9) is a key factor regulating the process of cartilage degeneration in OA.[53] In the Mn_1Ce_2-treated group, SOX9 expression was best preserved, suggesting retained capacity for cartilage matrix synthesis (Figure 3l). We stained chondrocytes cultured under different conditions for 24 h using Alcian Blue to assess the

https://doi.org/10.1021/acsnano.6c15540
ACS Nano XXXX, XXX, XXX−XXX

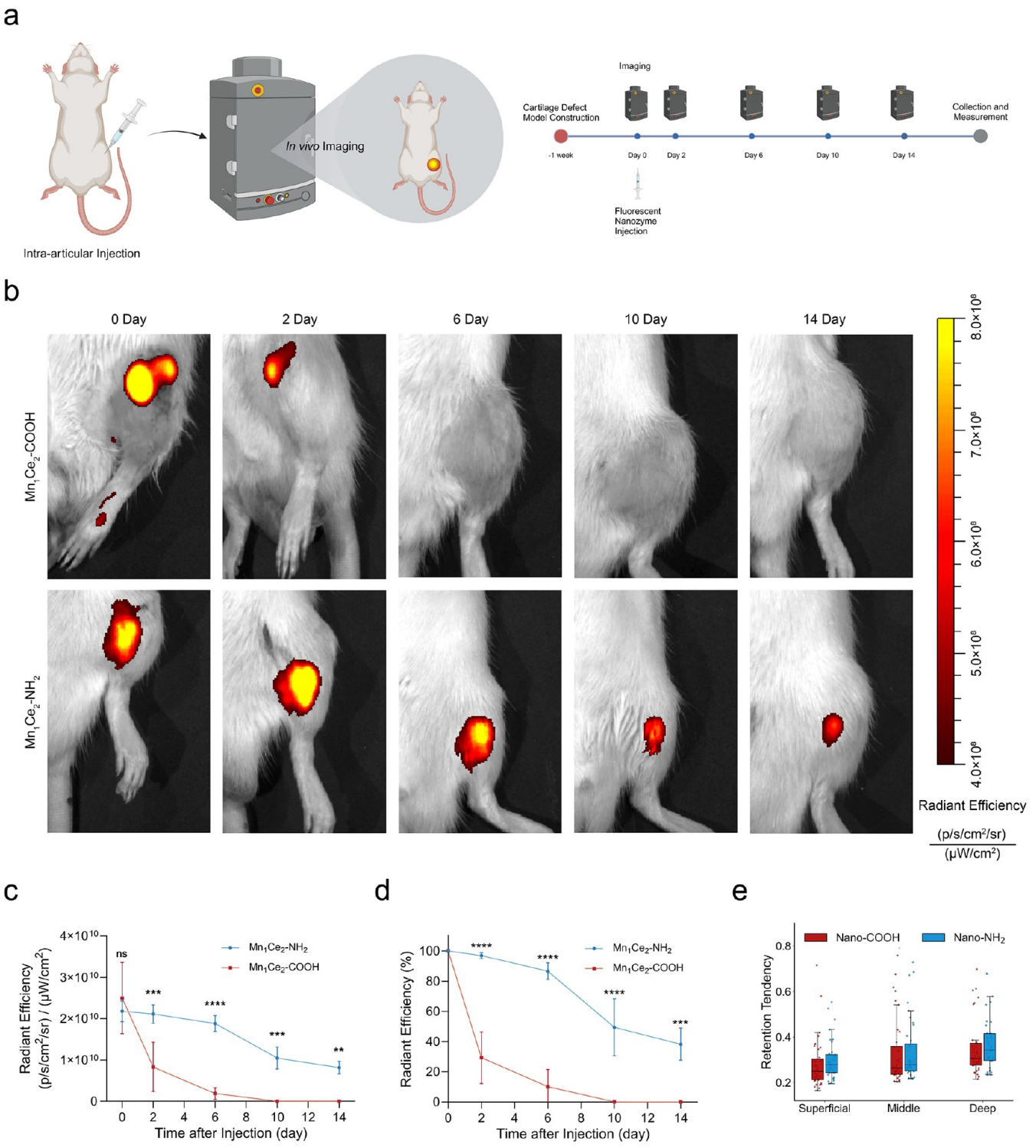

Figure 4. ***In vivo*** **effect of positive charge on retention time of nanozyme in joint. (a) Schematic for measuring the retention time of nanozymes in the rat knee joint. (b) IVIS images for rats after intra-articular injection with nanozymes with the progress of time. (c) Radiant efficiency and (d) radiant remaining ratio of the samples after intra-articular injection calculated from panel b. (e) Retention tendency of nanozymes by CGMD simulations in cartilage across superficial, middle, and deep layers. Data are presented as mean ± standard error of the mean (*n* = 3). Statistical analysis was performed using one-way ANOVA, **p* < 0.05, ***p* < 0.01, ****p* < 0.001, *****p* < 0.0001.**

synthesis of GAGs by chondrocytes.[54] As observed from the percentage of blue area of the staining, Mn_1Ce_2 restored the ability of chondrocytes to synthesize GAGs (Figure 3m,n). In addition, by using immunofluorescence we evaluated the expression of collagen type II α 1 (COL2A1), the main component of articular hyaline cartilage, and MMP13 in chondrocytes (Figure 3o,q).[55] Mn_1Ce_2 significantly enhanced the expression of COL2A1 and reduced the expression of MMP13 (Figure 3p,r).

In summary, Mn_1Ce_2 possessed the ability to eliminate ROS and inhibit macrophage M1 polarization. Moreover, it could protect chondrocytes under inflammatory conditions, restore

https://doi.org/10.1021/acsnano.6c15540
ACS Nano XXXX, XXX, XXX−XXX

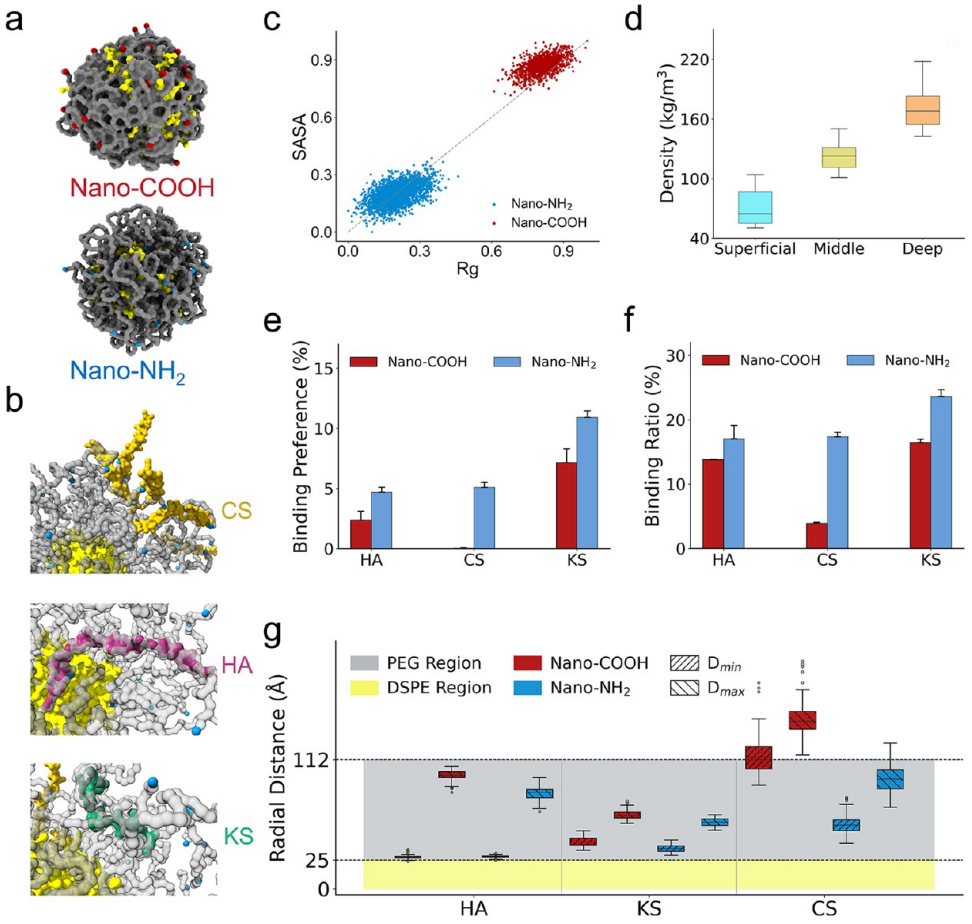

Figure 5. CGMD simulations of interactions between nanozymes and GAGs. (a) Representative snapshots of nanozymes, showing DSPE (yellow), PEG (gray), −COOH (red), and $-NH_2$ (blue). (b) In system composed of the nano-NH_2 and deep layer, CS (light brown) binds to nanozyme surface, HA (purple) spans across the PEG layer, and KS (green) embeds within PEG layer. (c) Conformational distribution of nanozymes, with R_g (radius of gyration) and SASA (solvent-accessible surface area) extracted from trajectories spanning 100−200 ns and subjected to min-max normalization. (d) Density distribution of GAG-based cartilage model, comprising superficial, middle, and deep layers. (e) Binding preference analysis showing preferential interactions of simulated nanozymes with HA, CS, and KS in deep layer, along with (f) complementary binding ratio experiment. (g) Binding modes between GAGs and nanozymes, derived from trajectories of mixed systems containing nanozymes and individual GAG types during 200−300 ns. D_{min} represents the minimum radial distance from GAG to nanozyme center, while D_{max} denotes the maximum radial distance.

their anabolism and inhibit their catabolism. The overall effect was better than that of undoped CeO_2.

In Vivo Effect of Positive Charge on Retention Time of Nanozyme in the Joint Cavity

To evaluate the retention time of Cy5.5-labeled nanozyme in rat joint cavities, the *in vivo* imaging system (IVIS) was used to detect changes in fluorescence intensity over time (Figure 4a). The fluorescence excitation spectrum of the nanozyme was measured using a microplate reader to confirm its successful functionalization with Cy5.5 (Figure S18). Mn_1Ce_2 modified with amino groups was designated as the positively charged nanozyme, whereas Mn_1Ce_2 modified with carboxyl groups was designated as the negatively charged nanozyme (Figure S19). After intra-articular injection, the fluorescence signals generated by nanozymes decreased with time. However, the decrease of the fluorescence signal of positively charged nanozyme was significantly slower than that of negatively charged nanozyme. The negatively charged nanozyme was no longer detectable by day 6, whereas the positively charged nanozyme exhibited prolonged retention for more than 14 days (Figure 4b). We quantified the radiant efficiency and the percentage of the initial radiant efficiency retained over time based on the IVIS results (Figure 4c,d). After 2 days, the radiant efficiency of the negatively charged nanozyme group had been reduced to less than half, with 29.31% of the initial signal remaining. For the positively charged nanozyme group, the radiant efficiency remained at approximately 1×10^{10} on day 10, with 49.48% of the initial signal remaining. As a result, the retention half-life of the positively charged nanozyme was 5−10-fold longer than that of the negatively charged counterpart. Based on the administered dose, the Mn loading, and the cumulative Mn ions release, the joint-volume-normalized Mn ion exposure was roughly estimated to be 0.4−0.6 μg/mL (Figure S15). Notably, this range encompasses the previously reported 0.5 μg/mL Mn ions concentration associated with favorable chondrocyte viability and enhanced expression of chondrogenic markers, including SOX9 and collagen II.[56] These results suggest that the prolonged intra-articular retention of the positively charged nanozyme may enable sustained Mn ion exposure within a range favorable for cartilage regeneration.

To elucidate the molecular mechanism underlying the surface charge-dependent retention of nanozymes in cartilage,

https://doi.org/10.1021/acsnano.6c15540
ACS Nano XXXX, XXX, XXX−XXX

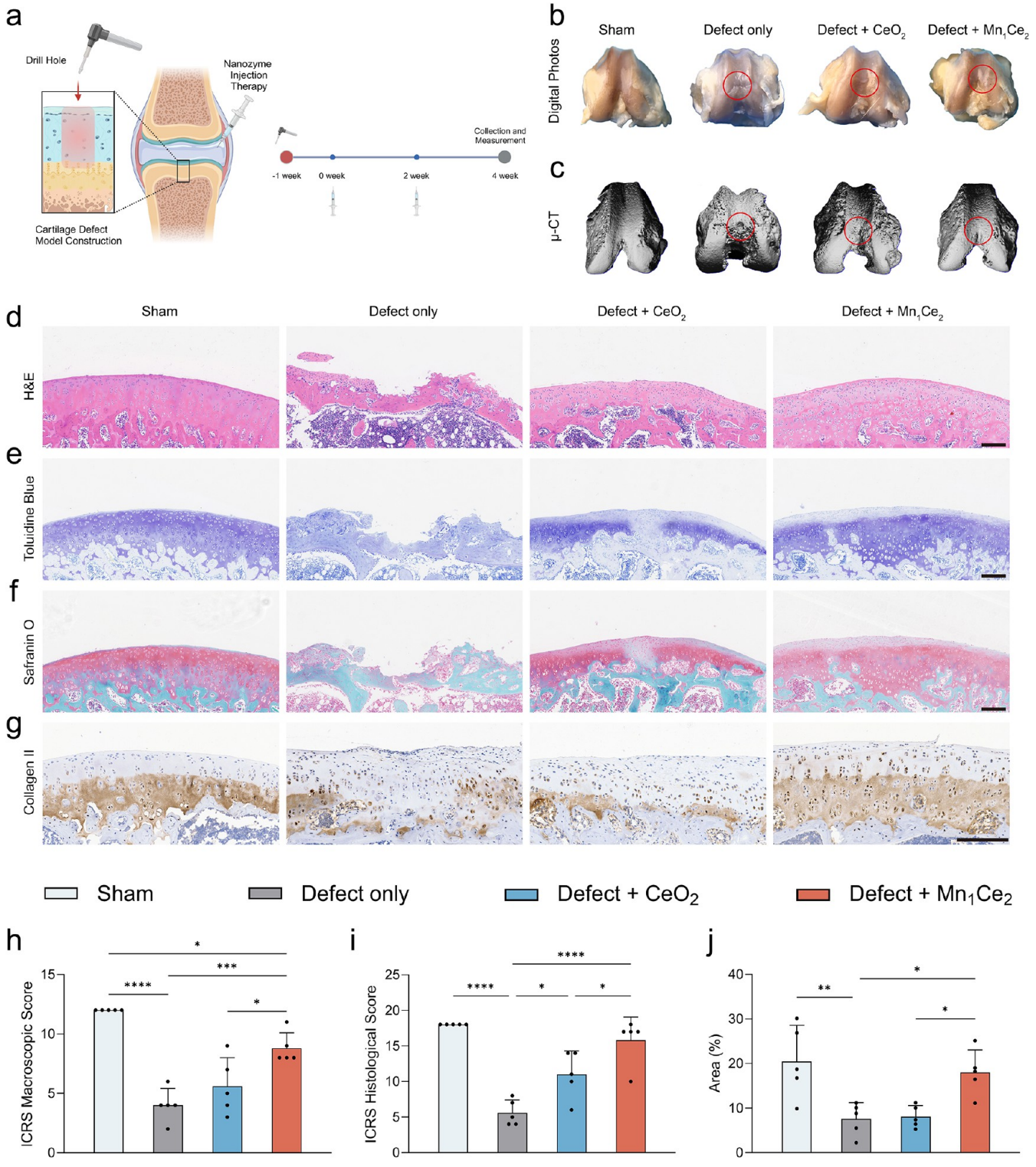

Figure 6. ***In vivo*** **OA treatment with Mn-doped CeO_2 nanozyme. (a) Schematic of *in vivo* OA treatment. (b) Digital photos of cartilage after 4 weeks with different treatments. The red circles show the location of the original cartilage defects. (c) Reconstruction of the bone on femurs using μ-CT. The red circles show the location of the original defects. (d) H&E staining, (e) Toluidine blue staining, (f) Safranin O/fast green staining and (g) collagen II staining to evaluate the articular cartilage regeneration (scale bar: 200 μm). (h) ICRS macroscopic evaluation. (i) ICRS histological evaluation. (j) Quantitative results of collagen II expression. Data are presented as mean $\pm$ standard error of the mean (n = 5). Statistical analysis was performed using one-way ANOVA, *p < 0.05, **p < 0.01, ***p < 0.001, ****p < 0.0001.**

we constructed nanozyme models with diameters of approximately 6 nm based on the experimental characterization (Figure 1j) for CGMD simulations, namely Nano-COOH and Nano-NH_2, representing carboxyl-functionalized negatively charged and amino-functionalized positively charged nanozymes, respectively (Figures 5a, S20, and S21). Articular cartilage models representing the superficial, middle, and deep layers were also established according to their respective GAG

https://doi.org/10.1021/acsnano.6c15540
ACS Nano XXXX, XXX, XXX−XXX

densities (Figures S22 and S25; Tables S3 and S4).[57] The Nano-COOH has a slightly larger diameter (≈5.99 nm) compared to Nano-NH_2 (≈5.96 nm), and the cartilage density follows the trend: superficial < middle < deep (Figure 5c,d). Subsequently, we performed CGMD simulations on 12 hybrid systems, combining Nano-NH_2 and Nano-COOH with HA, KS, CS, and the three GAG density layers. CGMD simulation results indicate that, compared with Nano-COOH, Nano-NH_2 exhibits a stronger retention tendency within cartilage, and this tendency increases with cartilage density (Figure 4e).

The denser three-dimensional network structure of the deep layer of cartilage provides a more favorable environment for nanozyme retention. Therefore, positively charged nanozymes are likely to achieve better therapeutic efficacy in the deep cartilage layer. These CGMD results provide a mechanistic basis for the experimentally observed prolonged retention of positively charged nanozymes, suggesting that enhanced electrostatic interactions with the negatively charged cartilage extracellular matrix contribute to their sustained retention within the joint cavity.

Molecular Mechanism of Nanozyme Retention in Cartilage

To elucidate how surface charge regulates nanozyme retention within cartilage at the molecular level, we performed CGMD simulations and systematically analyzed the binding preferences and binding modes of Nano-NH_2 and Nano-COOH with different GAGs (Figure 5b,5e−g). Under deep layer conditions, Nano-NH_2 exhibited significantly higher binding preference for GAGs compared to Nano-COOH, with the CS showing markedly greater enhancement than HA and KS (Figure 5e). To validate the binding preferences of the nanozyme toward the three types of GAGs observed in the simulations, we developed a magnetically-based sorting system. Specifically, after co-incubating magnetic oxide nanozymes with fluorescently labeled GAGs, we used a magnetic field to enrich the nanozymes bound to the GAGs and calculated the binding ratios of each GAG to the nanozymes based on the fluorescence ratio. The GAG binding ratios observed in the experimental results are consistent with the simulated trends (Figure 5f). These results suggested that CS served as the key GAG type mediating the prolonged retention of Nano-NH_2 within cartilage.

Additionally, the binding preference was not consistently higher for Nano-NH_2 compared to Nano-COOH across each type of GAG in the superficial and middle layers (Figure S36). This phenomenon may be attributed to the potential competitive binding between HA and CS with nanozymes, which is collectively regulated by electrostatic interactions, steric hindrance of GAGs (CS > KS > HA), and their density. For example, an inverse correlation was observed between the binding preferences of HA and CS toward nanozymes, wherein enhanced binding preference of HA toward nanozymes was accompanied by reduced binding preference of CS toward nanozymes (Figure S36), indicative of competitive binding dynamics between these two GAGs. In contrast, the binding preference of KS toward nanozymes appears to be predominantly governed by electrostatic interactions and cartilage density. Specifically, KS exhibits higher binding preference for Nano-NH_2 than for Nano-COOH, following the trend: superficial < middle < deep layer (Figures 5e, and S36). Binding ratio experiments of GAGs with nanozymes further indicate a potential competitive binding between HA and CS (Figure S46). Nevertheless, considering the overall trend, Nano-NH_2 still demonstrated greater binding preference for GAGs than Nano-COOH.

To elucidate the interplay among these contributions, electrostatic interactions, van der Waals forces, and steric effects, we further analyzed the interaction modes between nanozymes and GAGs. The binding modes of GAGs with nanozymes include traversing the PEG region, embedding into the PEG region, surface contact, and no binding (Figure 5b,g, and Table S5). Simulation results show that both HA and KS can bind to Nano-COOH, primarily by traversing and embedding into the PEG region; in the Nano-NH_2 system, this binding mode is further enhanced due to electrostatic attraction (Figure 5g). In contrast, the interaction between CS and Nano-COOH was typically limited to surface contact with the PEG region, or even no binding at all. This phenomenon, in addition to electrostatic repulsion, may also arise from the greater molecular weight of CS, which creates a steric hindrance effect. Notably, our simulations demonstrate that CS embeds within the PEG region of Nano-NH_2 *via* a mechanism in which strong electrostatic attraction effectively overcomes steric hindrance to establish a robust and stable binding configuration. This finding further indicates that CS is a critical GAG molecule in regulating the retention behavior of positively charged nanozymes in cartilage.

In Vivo OA Treatment with Mn-Doped CeO_2 Nanozyme

Based on the therapeutic effects of nanozymes at the cellular level and the beneficial impact of positive charge modification on their retention within the joint cavity, we further investigated the therapeutic effects of nanozymes in OA. A cartilage defect model was established by producing a defect (diameter: 2 mm, depth: 3 mm) at the femoral trochlear groove of the left knee of SD rats (Figure S47). Then, after 1 week, 15 rats with cartilage injury were randomly divided into three groups (n = 5) and intra-articularly injected with saline (Defect only group) or an equal volume of saline containing nanozymes. In addition, a sham operation was performed on five rats (Sham group) for comparison. Based on the above study of retention time, we scheduled two drug injections during the 4-week treatment period to ensure that the nanozyme concentration was maintained at therapeutically effective levels. At week 5 after surgery, the left femur tissues of 20 rats were harvested and analyzed with different methods (Figure 6a). These methods include macroscopic evaluation, subchondral bone evaluation and histological evaluation.

As shown in the macroscopic view, markedly incomplete repair of the cartilage defect was observed in the Defect only group (Figure 6b). Intra-articular administration of both nanozymes promoted filling of the cartilage defect. In particular, more intact cartilage in the defect area was observed in the Mn_1Ce_2 nanozyme treatment group, whose color and texture were similar to those of the Sham group. We further assessed the health of knee cartilage based on International Cartilage Repair Society (ICRS) macroscopic evaluation (Table S6).[58] Compared to the CeO_2 treated group and the Defect only group, the Mn_1Ce_2 treated group showed significant higher macroscopic repair scores (Figures 6h and S48).

The subchondral bone in the joint cavity provides support and elasticity, reducing the impact on the cartilage during joint loading.[59] According to the μ-CT images, Mn_1Ce_2 nanozyme treatment led to more intact reconstruction of subchondral bone in the defect area than Defect only group (Figure 6c). In

https://doi.org/10.1021/acsnano.6c15540
ACS Nano XXXX, XXX, XXX−XXX

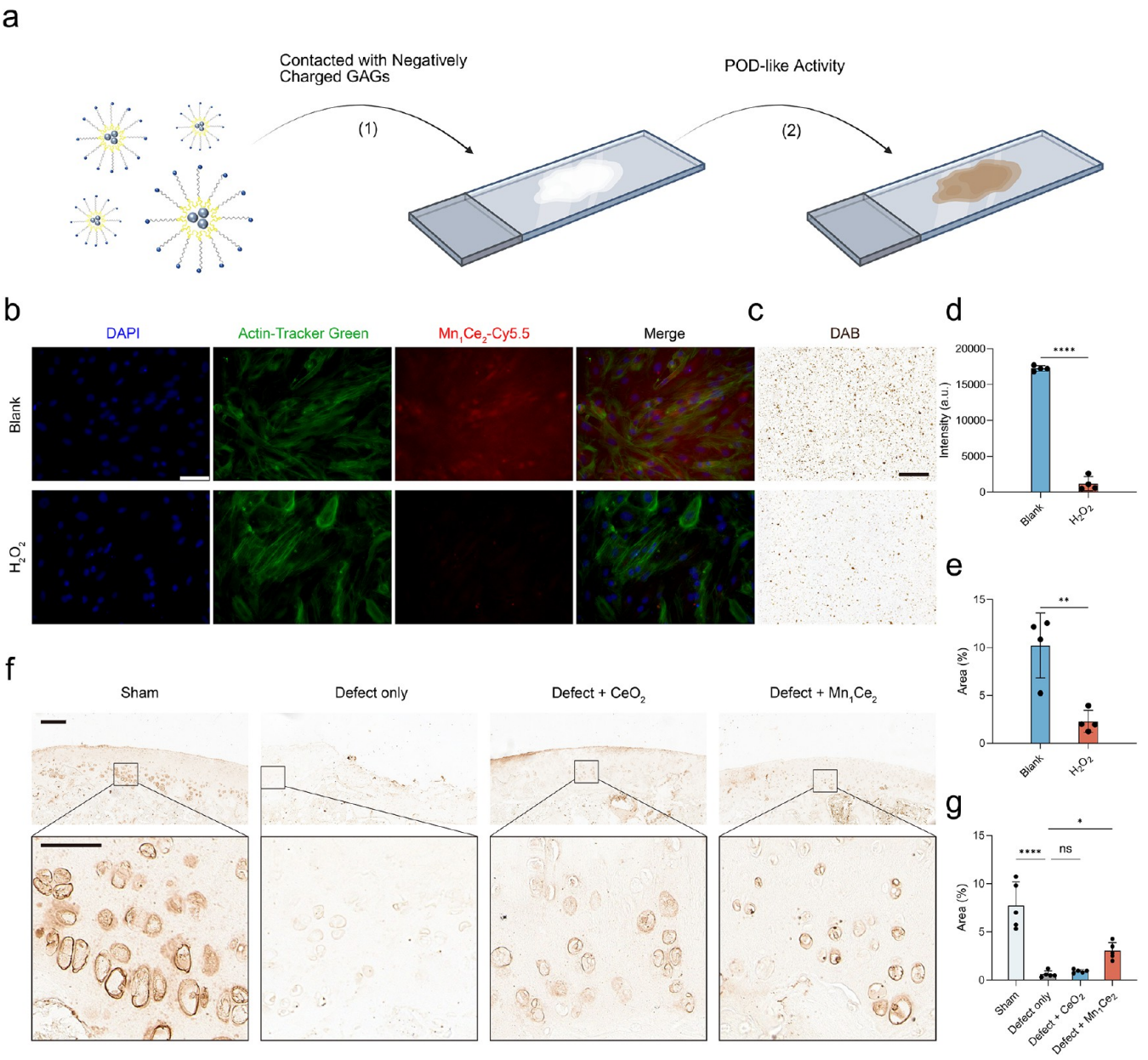

Figure 7. ***In vitro*** **diagnostic performance of Mn-doped CeO_2 nanozyme. (a) Schematic illustration of GAGs staining *via* the POD-like activity of nanozyme. (b) Images of chondrocytes after adsorption of fluorescently labeled nanozyme (scale bar: 100 μm). (c) Images of chondrocytes after DAB reaction catalyzed by nanozyme (scale bar: 200 μm). (d) Quantitative results of Mn_1Ce_2-Cy5.5 corresponding to panel b (n = 4). (e) Quantitative results of brown precipitate formed by DAB reaction corresponding to panel c (n = 4). (f) Images of cartilage after staining with nanozyme and DAB (scale bars: 200 μm and 50 μm). (g) Quantitative results of brown-positive areas corresponding to panel f (n = 5). Data are presented as mean ± standard error of the mean. Statistical analysis was performed using one-way ANOVA, *p < 0.05, **p < 0.01, ***p < 0.001, ****p < 0.0001.**

addition, we observed significant bone remodeling and bone erosion in the subchondral bone of the Defect only group, likely resulting from the osteoarthritic microenvironment induced by the cartilage defect. Both nanozyme treatments led to a reduction in bone erosion, but the effects were more significant in the Mn_1Ce_2 group.

For histological evaluation, Hematoxylin and Eosin (H&E) was used to assess tissue morphology, inflammatory infiltration, and cell death. As shown in Figure 6d, cartilage defect induction resulted in cartilage disruption and surface irregularity, which subsequently led to OA progression and extensive cell death. Nanozyme treatment alleviated this process. The location of the defect after 4 weeks of treatment showed tissue filling. Toluidine blue staining and Safranin O/fast green staining were used to assess the status of hyaline cartilage between different groups (Figure 6e,f).[60,61] The tissue regenerated in the CeO_2 treatment group was GAG-poor and resembled fibrotic scar tissue (Figure S49). In the Mn_1Ce_2 nanozyme treatment group, the regenerated tissue in the defect area integrated well with the surrounding native cartilage. Additionally, the regenerated tissue was rich in GAGs and contained abundant rounded, chondrocyte-like cells. Based on the μ-CT and tissue section results, we assessed cartilage regeneration using the ICRS visual histological assessment scale (Table S7).[62] In particular, the score of the Mn_1Ce_2 nanozyme treatment group was closest to that of the Sham

https://doi.org/10.1021/acsnano.6c15540
ACS Nano XXXX, XXX, XXX−XXX

group (Figures 6i and S50). Its results of μ-CT showed less subchondral bone remodeling and cartilage calcification. Its results of tissue sections showed better surface smoothness, more hyaline cartilage regeneration tissue, and more cellular distribution. On the other hand, collagen is the most abundant component of the cartilage extracellular matrix, accounting for approximately two-thirds of its dry weight.[63] We used immunohistochemical staining to assess collagen II content of cartilage tissue in the sections (Figure 6g). Quantitative results showed that collagen II in cartilage matrix was significantly increased after Mn_1Ce_2 nanozyme treatment (Figure 6j). Together, these results demonstrated the capacity of Mn_1Ce_2 nanozyme for cartilage and bone regeneration.

Meanwhile, after treatment, H&E staining of major organs (heart, liver, spleen, lung, and kidney) revealed no obvious histological changes or inflammatory damage, indicating good *in vivo* biocompatibility of CeO_2 and Mn_1Ce_2 nanozymes (Figure S51). In addition, the biodistribution and clearance of the Mn_1Ce_2 in major organs was evaluated within 28 days after intra-articular knee injection (Figure S52). The results showed that Mn_1Ce_2 is primarily metabolized by the liver. Within 28 days, the liver accounted for the clearance of approximately 60% of Mn_1Ce_2, further demonstrating its overall safety.

In Vitro Diagnostic Performance of Mn-Doped CeO_2 Nanozyme

The pathological diagnosis remains the gold standard for many diseases and is critical to evaluate the efficacy of therapeutics. While nanozymes have been widely used for bioanalysis, their use in pathological diagnosis has been much less explored. Previously, an iron oxide nanozyme with peroxidase (POD)-like activity was developed for *in vitro* cancer diagnosis.[64] In this study, the Mn_1Ce_2 nanozyme exhibited high POD-like activity as well (Figure S53). Enzyme kinetic analysis showed that the V_{max} of POD-like activity of Mn_1Ce_2 increased 20.5-fold compared with that of CeO_2 (Figure S54). Meanwhile, abundant negatively charged GAGs in cartilage correlate with the disease state of cartilage.[65] Detecting changes in the GAG content of cartilage is key to diagnosing cartilage regeneration. We have demonstrated that positively charged-modified nanozymes can effectively bind to the three major glycosaminoglycans in cartilage. By taking advantage of the positively charged property of Mn_1Ce_2 nanozyme, we reasoned that the nanozyme could accumulate at negatively charged GAGs and visualize the content of GAGs in cells or cartilage matrix. The staining process is shown in Figure 7a. The nanozyme catalyzed the 3,3'-diaminobenzidine tetrahydrochloride (DAB) to produce an insoluble brown product through POD-like activity (Figure S55).

To verify whether Mn_1Ce_2 can effectively bind to negatively charged GAGs and further catalyze the staining reaction, at the cellular level, we co-incubated Mn_1Ce_2 with chondrocytes containing different levels of GAGs (Figure 7b,d). The results showed that the Blank group, which contained a higher concentration of negatively charged GAGs, accumulated more Mn_1Ce_2, exhibited stronger red fluorescence, and demonstrated partial colocalization with the cells. In contrast, the H_2O_2 group exhibited weaker fluorescence signals. Furthermore, we co-incubated DAB with this system (Figure 7c,e). The results showed that the Blank group produced a more significant brown precipitate, proving that Mn_1Ce_2 bound to the cells effectively exerted its POD-like activity and successfully visualized the differences in GAG content among the groups.

At the level of the cartilage matrix, we used Mn_1Ce_2 to stain tissue sections obtained from *in vivo* experiments. As shown in Figure 7f, a large number of strongly positive cells were observed in the Sham group. In contrast, in the Defect only group, there were almost no chondrocytes at the defect site, and the surrounding chondrocytes showed almost little brown staining, indicating low GAG content. The CeO_2 treated and Mn_1Ce_2 treated groups alleviated the loss of GAGs, showing positively stained chondrocytes. In particular, a small amount of highly positive staining was also present in the Mn_1Ce_2-treated group, suggesting its regenerative potential. We evaluated the percentage of brown-positive areas using a quantitative method similar to immunohistochemistry, showing similar trends (Figure 7g). Similarly, 3-Amino-9-ethylcarbazole (AEC) was used to produce the visual red precipitate (Figure S56). As shown in Figure S57, the red precipitate possessed a more pronounced contrast to visualize the cartilage layer. The uneven staining of the cartilage layer was observed in the Defect only group, which could be attributed to the overall effect of the inflammatory environment on the cartilage matrix. Among the approaches for evaluating the health status of cartilage, visualization of collagen II using immunohistochemistry is costly and time-consuming. GAGs staining with Safranin O is difficult to quantify (Figure S58). In contrast, GAGs staining using Mn-doped CeO_2 nanozyme is cost-effective, time-saving, and quantitative. In summary, Mn-doped CeO_2 nanozyme also shows considerable potential for assessing the disease state of cartilage injury.

CONCLUSIONS

Our study established a rational design strategy for oxygen vacancy modulation in nanozymes through controlled elemental doping, offering mechanistic insights into enhanced therapeutic performance. The Mn_1Ce_2 nanozyme, engineered with high oxygen vacancy content, exhibited a synergistic combination of superior SOD- and CAT-like activities and exceptional biocompatibility, effectively protecting macrophages and chondrocytes from inflammatory damage. This structure-activity relationship arises from low-valence Mn doping, which tailors the electronic configuration and surface reactivity of CeO_2 nanozymes to amplify ROS scavenging activities. Importantly, the cationic surface functionality enabled sustained intra-articular retention, reducing dosing frequency while potentiating cartilage regeneration. Furthermore, we developed a pathological assay with Mn-doped CeO_2 to evaluate the healthy state of cartilage after therapy. In comparison with existing research on nanozyme-based diagnostic and therapeutic approaches, our study is one of the first to reveal an integrated model for the treatment and diagnosis of OA, positioning Mn-doped CeO_2 nanozymes as a versatile theranostic toolkit for OA management (Table S8). This work not only advances defect engineering principles in nanozyme design but also provides a basis for the development of next-generation theranostic platforms in regenerative medicine.

Furthermore, CGMD simulations indicated that cationic surface modification of nanozymes could enhance therapeutic efficacy in deeper cartilage layers, with CS emerging as the predominant GAG species mediating sustained intra-cartilaginous retention of cationic nanozymes. Beyond electrostatic differences, our findings suggest that the size of nanozymes

https://doi.org/10.1021/acsnano.6c15540
ACS Nano XXXX, XXX, XXX−XXX

may also play a critical role in modulating their retention behavior, thereby influencing the overall intra-articular retention efficacy. As an initial step, we performed exploratory simulations and experiments using smaller nanozymes to investigate the potential influence of particle size on retention behavior (Figures S35, S59, and Table S5). Future work will be directed toward systematically expanding this line of inquiry to optimize nanozyme design for enhanced OA treatment.

However, we acknowledge several current limitations: the diagnosis is restricted to *ex vivo* tissues and has not yet been translated to *in vivo* imaging (*e.g.*, MRI, photoacoustic, or fluorescence imaging); real-time monitoring of therapeutic responses remains lacking; and the current readout is solely colorimetric without multimodal imaging integration. Given that OA progression involves both molecular alterations in the cartilage matrix and structural changes in cartilage and subchondral bone, combining molecularly sensitive imaging with structural imaging could provide complementary information for more comprehensive pathological assessment and longitudinal monitoring of therapeutic responses. Although fluorescence imaging offers high sensitivity and the potential for real-time visualization, its limited tissue penetration may constrain its application to deep joints, particularly in humans. Near-infrared, especially NIR-II, fluorescence imaging may partially overcome this limitation by improving tissue penetration and reducing background autofluorescence. Nevertheless, integration with complementary modalities such as MRI or photoacoustic imaging may be required to achieve more reliable anatomical localization and *in vivo* diagnostic assessment. Addressing these issues—particularly by engineering imageable nanozyme variants and establishing feedback between diagnostic signals and therapeutic outcomes—will be a major focus of our future work and may ultimately help realize the full theranostic potential of nanozymes in OA management.

METHODS

Synthesis of Mn_xCe_y Nanozymes

The synthesis of Mn_xCe_y nanozymes (x:y = 3:2, 1:1, 1:2, 1:4, 1:8, and 0:1) was synthesized as shown below. Briefly, different ratios of cerium(III) acetylacetonate hydrate to manganese(III) acetylacetonate hydrate (the total mass was 0.5 g) were added to 15 mL of oleylamine. The mixture was heated to 110 °C, which started at 30 °C with a heating rate of 2 °C/min. Then, the mixture was maintained at 110 °C for 24 h. After obtaining a colloidal solution and cooling to room temperature, the Mn_xCe_y nanozymes were washed with acetone and collected by centrifugation. The six Mn_xCe_y nanozymes were named Mn_3Ce_2, Mn_1Ce_1, Mn_1Ce_2, Mn_1Ce_4, Mn_1Ce_8, and CeO_2, respectively. Next, 2 mL of the sample in chloroform (10 mg/mL) was mixed with 2 mL of DSPE-PEG-NH_2 in chloroform (20 mg/mL). The chloroform was removed by vacuum. Then, the nanozymes were dispersed in water.

Measurement of CAT-like Activity

The CAT-like activity of Mn_xCe_y nanozymes was measured by monitoring the amount of O_2 generated with a dissolved oxygen meter (SevenExcellence Multiparameter, Mettler Toledo Co. Ltd.). The nanozyme sample was mixed with H_2O_2 (final concentration: 50 mM). Immediately, the amount of O_2 was recorded by using a dissolved oxygen meter every 30 seconds.

Measurement of SOD-like Activity

The SOD-like activity of Mn_xCe_y nanozymes was assessed by using a SOD assay kit. First, 20 μL of the sample was mixed with 200 μL of 2-(4-iodophenyl)-3-(4-nitrophenyl)-5-(2,4- disulfophenyl)-2H-tetrazolium, monosodium salt. Next, 20 μL of the enzyme working solution was added to the mixture and cocultured at 37 °C for 20 min. Finally, the absorbance at 450 nm was recorded by using a microplate reader.

Measurement of POD-like Activity

The POD-like activity of Mn_xCe_y nanozymes was assessed based on the reaction of nanozyme catalyzing the oxidation of TMB to colored products by H_2O_2. The nanozyme sample was mixed with H_2O_2 (final concentration: 5 mM) and TMB (final concentration: 0.1 mM) in 0.2 M acetate buffer (pH = 4.0). The absorption changes of the reaction solutions at 652 nm were monitored by a spectrophotometer for 1 min.

In Vivo Retention of Nanozyme in Arthrography

Six SD rats (weighing 240-260 g) were randomly divided into two groups (n = 3). Solutions of amino- and carboxyl-coated nanozymes labeled Cy5.5 were prepared. Specifically, DSPE-PEG-Cy5.5 was modified on the surface of the nanozyme based on hydrophilic interaction. Each solution was injected intra-articularly in rats. At the set time point, the rats were imaged by an IVIS at the excitation wavelength of 680 nm and emission wavelength of 710 nm to determine the retention of injected materials.

Osteochondral Defect Surgical Procedure

The animal studies were approved by the Institutional Animal Care and Use Committee (IACUC) of Nanjing University (IACUC-2403011). Twenty SD rats (weighing 240-260 g) were randomly divided into four groups (Sham, Defect only, Defect+CeO_2 and Defect+Mn_1Ce_2) for *in vivo* experiments. Osteochondral defect surgery was performed on left knee of the animals. The knee joint of the rats was revealed by medial parapatellar arthrotomy, and the patella was displaced. In the trochlear groove of the femur, a osteochondral defect was drilled with a 2 mm diameter and 3 mm depth. Rats were anesthetized and injected with CeO_2 and Mn_1Ce_2 nanozymes in their joints after 1 and 3 weeks, respectively. After 5 weeks, the rats were dissected and tissue samples were collected.

ASSOCIATED CONTENT

Supporting Information

The Supporting Information is available free of charge at https://pubs.acs.org/doi/10.1021/acsnano.6c15540.

Experimental procedures for nanozyme characterization, *in vitro* and *in vivo* evaluation, molecular dynamics simulations, histological analysis, and statistical analysis; additional data on physicochemical properties, biological activity, cartilage targeting and repair, biodistribution and safety, and nanozyme−GAG interactions; primer sequences and simulation parameters (Figures S1−S59, and Tables S1−S8) (PDF)

AUTHOR INFORMATION

Corresponding Authors

Hao Dong − *State Key Laboratory of Analytical Chemistry for Life Science, School of Chemistry, Chemistry and Biomedicine Innovation Center (ChemBIC), ChemBioMed Interdisciplinary Research Center at Nanjing University and Kuang Yaming Honors School, & Institute for Brain Sciences, Nanjing University, Nanjing, Jiangsu 210023, China;* orcid.org/0000-0001-7280-7506; Email: donghao@nju.edu.cn

Hui Wei − *School of Biomedical Engineering, College of Engineering and Applied Sciences Nanjing National Laboratory of Microstructures, Jiangsu Key Laboratory of Artificial Functional Materials, Nanjing University, Nanjing, Jiangsu 210023, China; State Key Laboratory of Analytical Chemistry for Life Science, School of Chemistry, Chemistry and Biomedicine Innovation Center (ChemBIC),*

https://doi.org/10.1021/acsnano.6c15540
ACS Nano XXXX, XXX, XXX−XXX

ChemBioMed Interdisciplinary Research Center at Nanjing University, Nanjing University, Nanjing, Jiangsu 210023, China; orcid.org/0000-0003-0870-7142;
Email: weihui@nju.edu.cn

Authors

Dongze Mo − *School of Biomedical Engineering, College of Engineering and Applied Sciences Nanjing National Laboratory of Microstructures, Jiangsu Key Laboratory of Artificial Functional Materials, Nanjing University, Nanjing, Jiangsu 210023, China*

Yanbing Wen − *State Key Laboratory of Analytical Chemistry for Life Science, School of Chemistry, Chemistry and Biomedicine Innovation Center (ChemBIC), ChemBioMed Interdisciplinary Research Center at Nanjing University and Kuang Yaming Honors School, & Institute for Brain Sciences, Nanjing University, Nanjing, Jiangsu 210023, China;* orcid.org/0009-0004-9663-512X

Chaoqun Cheng − *School of Biomedical Engineering, College of Engineering and Applied Sciences Nanjing National Laboratory of Microstructures, Jiangsu Key Laboratory of Artificial Functional Materials, Nanjing University, Nanjing, Jiangsu 210023, China*

Xiwen Chen − *School of Biomedical Engineering, College of Engineering and Applied Sciences Nanjing National Laboratory of Microstructures, Jiangsu Key Laboratory of Artificial Functional Materials, Nanjing University, Nanjing, Jiangsu 210023, China*

Qi Sun − *School of Biomedical Engineering, College of Engineering and Applied Sciences Nanjing National Laboratory of Microstructures, Jiangsu Key Laboratory of Artificial Functional Materials, Nanjing University, Nanjing, Jiangsu 210023, China;* orcid.org/0009-0004-3613-2774

Hanjie Zhang − *School of Biomedical Engineering, College of Engineering and Applied Sciences Nanjing National Laboratory of Microstructures, Jiangsu Key Laboratory of Artificial Functional Materials, Nanjing University, Nanjing, Jiangsu 210023, China;* orcid.org/0009-0006-7174-7736

Xueying An − *State Key Laboratory of Pharmaceutical Biotechnology, Division of Sports Medicine and Adult Reconstructive Surgery, Department of Orthopedic Surgery, Nanjing Drum Tower Hospital, The Affiliated Hospital of Nanjing University Medical School, Nanjing University, Nanjing, Jiangsu 210008, China;* orcid.org/0009-0002-0882-623X

Wanling Liu − *School of Biomedical Engineering, College of Engineering and Applied Sciences Nanjing National Laboratory of Microstructures, Jiangsu Key Laboratory of Artificial Functional Materials, Nanjing University, Nanjing, Jiangsu 210023, China*

Xiaomiao Cui − *School of Biomedical Engineering, College of Engineering and Applied Sciences Nanjing National Laboratory of Microstructures, Jiangsu Key Laboratory of Artificial Functional Materials, Nanjing University, Nanjing, Jiangsu 210023, China;* orcid.org/0000-0002-5594-9390

Yihong Zhang − *School of Biomedical Engineering, College of Engineering and Applied Sciences Nanjing National Laboratory of Microstructures, Jiangsu Key Laboratory of Artificial Functional Materials, Nanjing University, Nanjing, Jiangsu 210023, China*

Quan Wang − *School of Biomedical Engineering, College of Engineering and Applied Sciences Nanjing National Laboratory of Microstructures, Jiangsu Key Laboratory of Artificial Functional Materials, Nanjing University, Nanjing, Jiangsu 210023, China*

Chenxin Zhu − *School of Biomedical Engineering, College of Engineering and Applied Sciences Nanjing National Laboratory of Microstructures, Jiangsu Key Laboratory of Artificial Functional Materials, Nanjing University, Nanjing, Jiangsu 210023, China*

Jiawei Li − *Department of Urology, Nanjing Drum Tower Hospital, The Affiliated Hospital of Nanjing University Medical School, Nanjing University, Nanjing, Jiangsu 210008, China*

Complete contact information is available at: https://pubs.acs.org/10.1021/acsnano.6c15540

Author Contributions

[#]D.M., Y.W., and C.C. contributed equally to this work.

Notes

The authors declare no competing financial interest.

■ ACKNOWLEDGMENTS

This work was funded by the National Natural Science Foundation of China (22374071 and W2512074), Jiangsu Provincial Key R&D Program (BE2022836), the National Key R&D Program of China (2021YFF1200700, 2019YFA0709200, and 2023YB3813001), State Key Laboratory of Analytical Chemistry for Life Science (5431ZZXM2501 and 5431ZZXM2306), the Fundamental Research Funds for the Central Universities (2026300425 and 202200325), and Yachen Foundation of Nanjing University. Parts of the calculations were performed using computational resources on an IBM Blade cluster system from the High-Performance Computing Center (HPCC) of Nanjing University.

■ REFERENCES

(1) Chen, M.; Chen, S.; Xie, C.; Li, F.; Tao, C.; Gong, W.; Qu, M.; Lin, S.; Shao, Z.; Xiao, G. Global prevalence, incidence, and years lived with disability (YLDs) of osteoarthritis: trends from 1990 to 2021 and projections to 2050. *J. Orthop. Transl.* **2026**, *56*, No. 101029.

(2) Macmull, S.; Skinner, J. A.; Bentley, G.; Carrington, R. W. J.; Briggs, T. W. R. Treating articular cartilage injuries of the knee in young people. *BMJ* **2010**, *340*, No. c998.

(3) Mahmoudian, A.; Lohmander, L. S.; Mobasheri, A.; Englund, M.; Luyten, F. P. Early-stage symptomatic osteoarthritis of the knee — time for action. *Nat. Rev. Rheumatol.* **2021**, *17*, 621−632.

(4) Bolduc, J. A.; Collins, J. A.; Loeser, R. F. Reactive oxygen species, aging and articular cartilage homeostasis. *Free Radical Biol. Med.* **2019**, *132*, 73−82.

(5) Katz, J. N.; Arant, K. R.; Loeser, R. F. Diagnosis and treatment of hip and knee osteoarthritis: a review. *J. Am. Med. Assoc.* **2021**, *325*, 568−578.

(6) Malda, J.; Groll, J.; van Weeren, P. R. Rethinking articular cartilage regeneration based on a 250-year-old statement. *Nat. Rev. Rheumatol.* **2019**, *15*, 571−572.

(7) Jones, I. A.; Togashi, R.; Wilson, M. L.; Heckmann, N.; Vangsness, C. T., Jr. Intra-articular treatment options for knee osteoarthritis. *Nat. Rev. Rheumatol.* **2019**, *15*, 77−90.

(8) Deng, R.; Zhao, R.; Zhang, Z.; Chen, Y.; Yang, M.; Lin, Y.; Ye, J.; Li, N.; Qin, H.; Yan, X.; Shi, J.; Yuan, F.; Song, S.; Xu, Z.; Song, Y.; Fu, J.; Xu, B.; Nie, G.; Yu, J.-K. Chondrocyte membrane−coated

nanoparticles promote drug retention and halt cartilage damage in rat and canine osteoarthritis. *Sci. Transl. Med.* **2024**, *16*, No. eadh9751.
(9) Larsen, C.; Østergaard, J.; Larsen, S. W.; Jensen, H.; Jacobsen, S.; Lindegaard, C.; Andersen, P. H. Intra-articular depot formulation principles: role in the management of postoperative pain and arthritic disorders. *J. Pharm. Sci.* **2008**, *97*, 4622−4654.
(10) Ng, L.; Grodzinsky, A. J.; Patwari, P.; Sandy, J.; Plaas, A.; Ortiz, C. Individual cartilage aggrecan macromolecules and their constituent glycosaminoglycans visualized via atomic force microscopy. *J. Struct. Biol.* **2003**, *143*, 242−257.
(11) Evans, C. H.; Kraus, V. B.; Setton, L. A. Progress in intra-articular therapy. *Nat. Rev. Rheumatol.* **2014**, *10*, 11−22.
(12) Stephens, M. B.; Beutler, A. I.; O'Connor, F. G. Musculoskeletal injections: a review of the evidence. *Am. Fam. Phys.* **2008**, *78*, 971−976.
(13) Chen, Y.; Sun, W.; Wen, Y.; Wang, X.; Li, J.; Xie, S.; Li, R.; Ma, Y.; Wu, H.; Zhu, Q.; Chen, Z.; Zhang, X.; Liao, Y.; Lin, J.; Li, W.; Yan, Y.; Ying, D.; He, Q.; Meng, H.; Teng, C.; Zhou, W.; Wang, Y.; Li, X.; Yin, Z.; Wei, W.; Leong, K. W.; Ouyang, H. A cationic polymer drives glycosaminoglycan assembly and secretion for preclinical osteoarthritis therapy. *Sci. Transl. Med.* **2025**, *17*, No. eadl5623.
(14) Rahimi, M.; Charmi, G.; Matyjaszewski, K.; Banquy, X.; Pietrasik, J. Recent developments in natural and synthetic polymeric drug delivery systems used for the treatment of osteoarthritis. *Acta Biomater.* **2021**, *123*, 31−50.
(15) Geiger, B. C.; Wang, S.; Padera, R. F.; Grodzinsky, A. J.; Hammond, P. T. Cartilage-penetrating nanocarriers improve delivery and efficacy of growth factor treatment of osteoarthritis. *Sci. Transl. Med.* **2018**, *10*, No. eaat8800.
(16) Lin, F.; Wang, Z.; Xiang, L.; Deng, L.; Cui, W. Charge-guided micro/nano-hydrogel microsphere for penetrating cartilage matrix. *Adv. Funct. Mater.* **2021**, *31*, No. 2107678.
(17) Lei, Y.; Wang, Y.; Shen, J.; Cai, Z.; Zhao, C.; Chen, H.; Luo, X.; Hu, N.; Cui, W.; Huang, W. Injectable hydrogel microspheres with self-renewable hydration layers alleviate osteoarthritis. *Sci. Adv.* **2022**, *8*, No. eabl6449.
(18) Wei, H.; Wang, E. Nanomaterials with enzyme-like characteristics (nanozymes): next-generation artificial enzymes. *Chem. Soc. Rev.* **2013**, *42*, 6060−6093.
(19) Wu, J.; Wang, X.; Wang, Q.; Lou, Z.; Li, S.; Zhu, Y.; Qin, L.; Wei, H. Nanomaterials with enzyme-like characteristics (nanozymes): next-generation artificial enzymes (II). *Chem. Soc. Rev.* **2019**, *48*, 1004−1076.
(20) Wang, Q.; Wei, H.; Zhang, Z.; Wang, E.; Dong, S. Nanozyme: An emerging alternative to natural enzyme for biosensing and immunoassay. *TrAC, Trends Anal. Chem.* **2018**, *105*, 218−224.
(21) Wei, H.; Gao, L.; Fan, K.; Liu, J.; He, J.; Qu, X.; Dong, S.; Wang, E.; Yan, X. Nanozymes: a clear definition with fuzzy edges. *Nano Today* **2021**, *40*, No. 101269.
(22) Liang, M.; Yan, X. Nanozymes: from new concepts, mechanisms, and standards to applications. *Acc. Chem. Res.* **2019**, *52*, 2190−2200.
(23) Ma, L.; Liang, Z.; Hou, Y.; Zhang, R.; Fan, K.; Yan, X. Nanozymes and their potential roles in the origin of life. *Adv. Mater.* **2025**, *37*, No. 2412211.
(24) Zhang, R.; Jiang, B.; Fan, K.; Gao, L.; Yan, X. Designing nanozymes for in vivo applications. *Nat. Rev. Bioeng.* **2024**, *2*, 849−868.
(25) Fu, X.; Yu, X.; Jiang, J.; Yang, J.; Chen, L.; Yang, Z.; Yu, C. Small molecule-assisted assembly of multifunctional ceria nanozymes for synergistic treatment of atherosclerosis. *Nat. Commun.* **2022**, *13*, No. 6528.
(26) Feng, Y.; Luo, X.; Li, Z.; Fan, X.; Wang, Y.; He, R.-R.; Liu, M. A ferroptosis-targeting ceria anchored halloysite as orally drug delivery system for radiation colitis therapy. *Nat. Commun.* **2023**, *14*, No. 5083.
(27) Peng, W.; Tai, W.; Li, B.; Wang, H.; Wang, T.; Guo, S.; Zhang, X.; Dong, P.; Tian, C.; Feng, S.; Yang, L.; Cheng, G.; Zheng, B. Inhalable nanocatalytic therapeutics for viral pneumonia. *Nat. Mater.* **2025**, *24*, 637−648.
(28) Yu, L.; Chang, J.; Zhuang, X.; Li, H.; Hou, T.; Li, F. Two-Dimensional Cobalt-Doped Ti_3C_2 MXene Nanozyme-Mediated Homogeneous Electrochemical Strategy for Pesticides Assay Based on In Situ Generation of Electroactive Substances. *Anal. Chem.* **2022**, *94*, 3669−3676.
(29) Gai, P.; Pu, L.; Wang, C.; Zhu, D.; Li, F. CeO_2@NC nanozyme with robust dephosphorylation ability of phosphotriester: A simple colorimetric assay for rapid and selective detection of paraoxon. *Biosens. Bioelectron.* **2023**, *220*, No. 114841.
(30) Soh, M.; Kang, D.-W.; Jeong, H.-G.; Kim, D.; Kim, D. Y.; Yang, W.; Song, C.; Baik, S.; Choi, I.-Y.; Ki, S.-K.; Kwon, H. J.; Kim, T.; Kim, C. K.; Lee, S.-H.; Hyeon, T. Ceria−zirconia nanoparticles as an enhanced multi-antioxidant for sepsis treatment. *Angew. Chem., Int. Ed.* **2017**, *56*, 11399−11403.
(31) Gallup, W. D.; Norris, L. C. The essentialness of manganese for the normal development of bone. *Science* **1938**, *87*, 18−19.
(32) Kamaraj, M.; Roopavath, U. K.; Giri, P. S.; Ponnusamy, N. K.; Rath, S. N. Modulation of 3D printed calcium-deficient apatite constructs with varying Mn concentrations for osteochondral regeneration via endochondral differentiation. *ACS Appl. Mater. Interfaces* **2022**, *14*, 23245−23259.
(33) Beattie, J. H.; Avenell, A. Trace element nutrition and bone metabolism. *Nutr. Res. Rev.* **1992**, *5*, 167−188.
(34) Strause, L.; Saltman, P. Role of Manganese in Bone Metabolism. In *Nutritional bioavailability of manganese*; Kies, C., Ed.; American Chemical Society, 1987; pp 46−55.
(35) Du, Z.; Leng, H.; Guo, L.; Huang, Y.; Zheng, T.; Zhao, Z.; Liu, X.; Zhang, X.; Cai, Q.; Yang, X. Calcium silicate scaffolds promoting bone regeneration via the doping of Mg^{2+} or Mn^{2+} ion. *Composites, Part B* **2020**, *190*, No. 107937.
(36) Takagi, J.; Petre, B. M.; Walz, T.; Springer, T. A. Global conformational rearrangements in integrin extracellular domains in outside-in and inside-out signaling. *Cell* **2002**, *110*, 599−611.
(37) Rohrmann, K.; Niemann, R.; Buddecke, E. Two N-acetylgalactosaminyltransferase are involved in the biosynthesis of chondroitin sulfate. *Eur. J. Biochem.* **1985**, *148*, 463−469.
(38) Zhang, P.; Lu, H.; Zhou, Y.; Zhang, L.; Wu, Z.; Yang, S.; Shi, H.; Zhu, Q.; Chen, Y.; Dai, S. Mesoporous $MnCeO_x$ solid solutions for low temperature and selective oxidation of hydrocarbons. *Nat. Commun.* **2015**, *6*, No. 8446.
(39) Gupta, A. K.; Kripal, R. EPR and photoluminescence properties of Mn^{2+} doped CdS nanoparticles synthesized via co-precipitation method. *Spectrochim. Acta, Part A* **2012**, *96*, 626−631.
(40) Sudarsanam, P.; Selvakannan, P. R.; Soni, S. K.; Bhargava, S. K.; Reddy, B. M. Structural evaluation and catalytic performance of nano-Au supported on nanocrystalline $Ce_{0.9}Fe_{0.1}O_{2-\delta}$ solid solution for oxidation of carbon monoxide and benzylamine. *RSC Adv.* **2014**, *4*, 43460−43469.
(41) Gong, J.; Meng, F.; Fan, Z.; Li, H.; Du, Z. Template-free controlled hydrothermal synthesis for monodisperse flowerlike porous CeO_2 microspheres and their superior catalytic reduction of NO with NH_3. *J. Alloys Compd.* **2017**, *690*, 677−687.
(42) Ma, X.; Lu, P.; Wu, P. Structural, optical and magnetic properties of CeO_2 nanowires with nonmagnetic Mg^{2+} doping. *J. Alloys Compd.* **2018**, *734*, 22−28.
(43) Tiwari, S.; Khatun, N.; Shrivastava, T.; Kumar, S.; Liu, S.-W.; Biring, S.; Sen, S. Structural, optical and mechanical properties of sol-gel synthesized Mn-doped CeO_2. *Superlattices Microstruct.* **2018**, *122*, 316−323.
(44) Shen, F.; Fang, Y.; Wu, Y.; Zhou, M.; Shen, J.; Fan, X. Metal ions and nanometallic materials in antitumor immunity: function, application, and perspective. *J. Nanobiotechnol.* **2023**, *21*, No. 20.
(45) Henrotin, Y. E.; Bruckner, P.; Pujol, J. P. L. The role of reactive oxygen species in homeostasis and degradation of cartilage. *Osteoarthr. Cartil.* **2003**, *11*, 747−755.

(46) Gordon, S.; Martinez, F. O. Alternative activation of macrophages: mechanism and functions. *Immunity* **2010**, *32*, 593−604.
(47) Kapoor, M. Pathogenesis of Osteoarthritis. In *Osteoarthritis: Pathogenesis, Diagnosis, Available Treatments, Drug Safety, Regenerative and Precision Medicine*; Kapoor, M.; Mahomed, N. N., Eds.; Springer International Publishing: Cham, 2015; pp 1−28.
(48) Morales, T. I. Chondrocyte moves: clever strategies? *Osteoarthr. Cartil.* **2007**, *15*, 861−871.
(49) Qu, F.; Guilak, F.; Mauck, R. L. Cell migration: implications for repair and regeneration in joint disease. *Nat. Rev. Rheumatol.* **2019**, *15*, 167−179.
(50) Lianxu, C.; Hongti, J.; Changlong, Y. NF-κBp65-specific siRNA inhibits expression of genes of COX-2, NOS-2 and MMP-9 in rat IL-1β-induced and TNF-α-induced chondrocytes. *Osteoarthr. Cartil.* **2006**, *14*, 367−376.
(51) Wang, C.; Shen, J.; Ying, J.; Xiao, D.; O'Keefe, R. J. FoxO1 is a crucial mediator of TGF-β/TAK1 signaling and protects against osteoarthritis by maintaining articular cartilage homeostasis. *Proc. Natl. Acad. Sci. U.S.A.* **2020**, *117*, 30488−30497.
(52) Nagase, H.; Kashiwagi, M. Aggrecanases and cartilage matrix degradation. *Arthritis Res. Ther.* **2003**, *5*, No. 94.
(53) Zhang, Q.; Ji, Q.; Wang, X.; Kang, L.; Fu, Y.; Yin, Y.; Li, Z.; Liu, Y.; Xu, X.; Wang, Y. SOX9 is a regulator of ADAMTSs-induced cartilage degeneration at the early stage of human osteoarthritis. *Osteoarthr. Cartil.* **2015**, *23*, 2259−2268.
(54) Song, P.; Cui, Z.; Hu, L. Applications and prospects of intra-articular drug delivery system in arthritis therapeutics. *J. Controlled Release* **2022**, *352*, 946−960.
(55) Eyre, D. Articular cartilage and changes in arthritis: collagen of articular cartilage. *Arthritis Res. Ther.* **2002**, *4*, No. 30.
(56) Wei, L.; Qin, S.; Ye, Y.; Hu, J.; Luo, D.; Li, Y.; Gao, Y.; Jiang, L.; Zhou, Q.; Xie, X.; Li, N. Chondrogenic potential of manganese-loaded composite scaffold combined with chondrocytes for articular cartilage defect. *J. Mater. Sci.: Mater. Med.* **2022**, *33*, No. 74.
(57) Pueyo Moliner, A.; Ito, K.; Zaucke, F.; Kelly, D. J.; de Ruijter, M.; Malda, J. Restoring articular cartilage: insights from structure, composition and development. *Nat. Rev. Rheumatol.* **2025**, *21*, 291−308.
(58) van den Borne, M. P. J.; Raijmakers, N. J. H.; Vanlauwe, J.; Victor, J.; de Jong, S. N.; Bellemans, J.; Saris, D. B. F. International Cartilage Repair Society (ICRS) and Oswestry macroscopic cartilage evaluation scores validated for use in Autologous Chondrocyte Implantation (ACI) and microfracture. *Osteoarthr. Cartil.* **2007**, *15*, 1397−1402.
(59) van Weeren, P. R. 1-General Anatomy and Physiology of Joints. In *Joint disease in the horse*, 2nd ed.; McIlwraith, C. W.; Frisbie, D. D.; Kawcak, C. E.; van Weeren, P. R., Eds.; W.B. Saunders: Edinburgh, 2016; pp 1−24.
(60) Musumeci, G.; Castrogiovanni, P.; Mazzone, V.; Szychlinska, M. A.; Castorina, S.; Loreto, C. Histochemistry as a unique approach for investigating normal and osteoarthritic cartilage. *Eur. J. Histochem.* **2014**, *58*, No. 2371.
(61) Laverty, S.; Girard, C. A.; Williams, J. M.; Hunziker, E. B.; Pritzker, K. P. H. The OARSI histopathology initiative − recommendations for histological assessments of osteoarthritis in the rabbit. *Osteoarthr. Cartil.* **2010**, *18*, S53−S65.
(62) Mainil-Varlet, P.; Aigner, T.; Brittberg, M.; Bullough, P.; Hollander, A.; Hunziker, E.; Kandel, R.; Nehrer, S.; Pritzker, K.; Roberts, S.; Stauffer, E. Histological assessment of cartilage repair: a report by the histology endpoint committee of the International Cartilage Repair Society (ICRS). *J. Bone Joint Surg.* **2003**, *85*, 45−57.
(63) Eyre, D. R. Collagens and cartilage matrix homeostasis. *Clin. Orthop. Relat. Res.* **2004**, *427*, S118−S122.
(64) Fan, K.; Cao, C.; Pan, Y.; Lu, D.; Yang, D.; Feng, J.; Song, L.; Liang, M.; Yan, X. Magnetoferritin nanoparticles for targeting and visualizing tumour tissues. *Nat. Nanotechnol.* **2012**, *7*, 833.
(65) Lawson, T.; Joenathan, A.; Patwa, A.; Snyder, B. D.; Grinstaff, M. W. Tantalum oxide nanoparticles for the quantitative contrast-enhanced computed tomography of ex vivo human cartilage: assessment of biochemical composition and biomechanics. *ACS Nano* **2021**, *15*, 19175−19184.

https://doi.org/10.1021/acsnano.6c15540
ACS Nano XXXX, XXX, XXX−XXX